

# Quasi-matrix-free hybrid multigrid on dynamically adaptive Cartesian grids

Marion Weinzierl <sup>\*</sup>      Tobias Weinzierl <sup>†</sup>

July 19, 2017

## Abstract

We present a family of spacetree-based multigrid realizations using the tree’s multiscale nature to derive coarse grids. They align with matrix-free geometric multigrid solvers as they never assemble the system matrices which is cumbersome for dynamically adaptive grids and full multigrid. The most sophisticated realizations use BoxMG to construct operator-dependent prolongation and restriction in combination with Galerkin/Petrov-Galerkin coarse-grid operators. This yields robust solvers for nontrivial elliptic problems. We embed the algebraic, problem- and grid-dependent multigrid operators as stencils into the grid and evaluate all matrix-vector products in-situ throughout the grid traversals. While such an approach is not literally matrix-free—the grid carries the matrix—we propose to switch to a hierarchical representation of all operators. Only differences of algebraic operators to their geometric counterparts are held. These hierarchical differences can be stored and exchanged with small memory footprint. Our realizations support arbitrary dynamically adaptive grids while they vertically integrate the multilevel operations through spacetree linearization. This yields good memory access characteristics, while standard colouring of mesh entities with domain decomposition allows us to use parallel manycore clusters. All realization ingredients are detailed such that they can be used by other codes.

## 1 Introduction

Quadrees, octrees and their generalization, all covered by the term spacetree, are popular meshing paradigms in scientific computing, either for plain meshing or as building blocks within forests of trees [13, 31, 40, 42, 43, 49, 50, 58]. They offer a geometric multiscale hierarchy, they support in-situ meshing, they offer the opportunity to erase and refine parts of the grid easily, their structuredness facilitates efficient implementations, and fast domain decomposition methods are known for them—notably in combination with space-filling curves (SFCs) [4]. Therefore, they are well-suited for multigrid solvers for elliptic partial differential equations (PDEs) discretized by finite elements. Stagnating or decreasing memory per core, a widening memory gap and communication constraints hereby encourage the use of matrix-free multigrid [2]. Instead of assembling an equation system, all required matrix-vector multiplications (matvecs) are computed directly on the grid. No matrix allocation or maintenance costs arise.

---

<sup>\*</sup>Department of Mathematical Sciences, Durham University, UK. (marion.weinzierl@durham.ac.uk)

<sup>†</sup>School of Engineering and Computing Sciences, Durham University, UK. (tobias.weinzierl@durham.ac.uk)

Matvecs without assembly or storage of matrix entries require that all operators can efficiently be determined on-the-fly from the grid. In algebraic multigrid (e.g. [48] and references therein), inter-grid transfer (prolongation and restriction) and coarse-grid operators however depend recursively over several mesh levels on the PDE discretization. An on-the-fly computation requires the partial, repeated and redundant re-assembly of the system matrix entries in every solver sweep. Furthermore, algebraic methods derive the coarse grid from the operator characteristics, i.e. a good coarse grid anticipates the problem’s behaviour. The grid and its data structures are not given a priori. Geometric multigrid (e.g. [11] and references therein) in contrast is better suited for matrix-free, fast implementations as it fixes the grid hierarchy and hardcodes or prescribes the operators. Unfortunately, it quickly becomes unstable.

We use the convection-diffusion equation

$$-\nabla \cdot (\epsilon \nabla) u + (v \nabla) u = f \quad \text{on } \Omega = (0, 1)^d, u : \Omega \mapsto \mathbf{R} \quad (1)$$

as demonstrator, where the diffusion coefficient  $\epsilon$  is a rank-2 tensor with diagonal entries  $\epsilon_1, \dots, \epsilon_d$  and the convection velocities  $v = (v_1, \dots, v_d)^T$  for  $d \in \{2, 3\}$ . It describes, for example, the transport of chemicals  $u$  in a fluid given by  $v$  or yields a precursor for the Navier-Stokes equations where  $v \mapsto u$  and  $f \mapsto f(u)$ . This equation is challenging for geometric multigrid if  $\epsilon$ ,  $v$  or—*not studied in the present work*—the shape of  $\Omega$  are non-trivial and if no particular/manual effort is invested to construct well-suited coarse grids. Algebraic multigrid, in contrast, can robustly and efficiently solve it as black box: Classic coarse grid identification places coarse grid points along material-/ $\epsilon$ -transitions, makes coarse grids anticipate anisotropies and convection, and it anticipates the domain layout. Classic multigrid operator construction takes the same triad into account. Both complement each other, i.e. sophisticated AMG makes the operators compensate weaker coarse grid choices and the other way round.

We see three approaches for combining the robustness of algebraic multigrid with the advantages of geometric multigrid. First, we can use the spacetree concept to define the grid hierarchy and the fine-grid discretization (stencils), but compute the coarse-grid operators and inter-grid transfer operators algebraically (not on-the-fly). An expensive coarse-grid/c-point identification phase, as necessary in algebraic multigrid through matching on graphs, e.g., is thus omitted. At the same time, the linear algebra subroutines and the memory allocation can take advantage of the structured grid. As a second possibility, we may couple a geometric and an algebraic multigrid code. On fine meshes, diffusion processes typically dominate while material parameters are reasonably smooth. Matrix-free geometric multigrid based on rediscrretization and fixed inter-grid operators yield reasonable convergence. On coarse meshes, one can employ algebraic multigrid, alternative iterative schemes or a direct solver. Such an approach [28, 35, 43, 49] is robust and fast at modest memory requirements as long as the finest algebraic problem with a matrix setup remains reasonably coarse within the grid hierarchy. Finally, we may also decide to tailor all operators to the problem manually and to hard-code it into the solver software. Inter-grid transfer operators, for example, can anticipate the  $\epsilon$  and  $v$  behaviour on finer meshes through homogenization. Such a strategy mirrors the fact that many engineers put significant effort into the creation of high-quality simulation grids. We fix the grid but invest into the operator. Such an approach does not work on-the-fly as black box.

In this paper, we present a fourth technique that merges the advantages of spacetrees plus rediscrretization with the robustness of algebraic multigrid: space-tree based multigrid using Petrov-Galerkin coarse-grid and operator-dependent inter-grid transfer operators. This allows us to solve significantly harder elliptic problems without matrix assembly than a classic geometric approach while we retain the advantages of geometric multigrid. On the one hand, our solvers do not increase

the memory footprint significantly and thus are a convenient building block for extreme scale simulations where the memory per core is a limiting factor. On the other hand, our solvers preserve the geometric structuredness of spacetrees which is an important characteristic for many optimisation techniques and domain decomposition approaches.

Our description consists of three parts. We start from an outline of the used tree data structures, grid traversal and terminology (Sect. 3). In Sect. 4 we then revisit three multigrid solver variants that fit to spacetrees and spacetree traversals: additive, BPX-type and multiplicative solvers [8] on hierarchical generating systems [30]. All work in a strictly element-wise multiscale sense, that is, they only require one cell or vertex record, respectively, plus their parents (next coarser entities) at a time, and they read each individual spacetree cell only once per multigrid smoothing step. This makes them well-prepared for future architecture with a widening memory gap [22]. We next introduce block Jacobi-type smoothers that preserve the tree’s single run-through policy, and we enhance the geometric multigrid implementation with element-wise Galerkin coarse-grid operators. These operators are embedded into the tree, that is, the grid acts both as an organizational and as a compute data structure. Galerkin coarse-grid operators improve the convergence rates, but the solver becomes really robust only once we use operator-dependent prolongation and restriction through Black Box Multigrid (BoxMG) [16, 17, 20]. BoxMG on locally refined grids for bipartitioning is known [47]. Our contribution is that we simplify its realisation on (dynamically) adaptive grids through the fusion of BoxMG with full approximation storage (FAS) [52] realized through HTMG [29]. Our code furthermore reduces the computation of BoxMG operators through mirroring all computations onto one reference configuration. This renders the programming of BoxMG, notably for  $d = 3$ , simpler than published by any other author.

Embedding all operators as stencils into the grid is not literally matrix-free. In the second part of the manuscript (Sect. 5), we thus replace the storage of the operators in the tree with a compressed encoding. We determine the difference of all operators to geometric rediscrretization or  $d$ -linear operators, respectively, and store only the hierarchical differences of algebraic to geometric stencils. In the best case, the difference is negligible and no floating point data is to be held at all. This reduces the memory footprint. We work almost matrix-free but preserve BoxMG’s robustness. To the best of our knowledge, such an approach to realize algebraic operators almost at the memory cost of rediscrretization-based multigrid is new.

The final part of the paper (Sect. 6) sketches a shared and distributed memory parallelization. The shared memory discussion derives data dependency graphs that can be fed into a task-based system [3]. The distributed memory discussion studies data flow characteristics for non-overlapping domain decompositions well-suited for MPI. For both parallelization variants we show that our approach is by construction well-suited for parallel machines; a property stemming from the strict element-wise data access.

Our contribution benefits from the fusion of three ingredients: Operator-dependent prolongation and restriction on dynamically adaptive spacetrees, stencil compression and concurrency analysis. These three parts introduce two notions of hybrid algebraic-geometric multigrid that are orthogonal to the classic notion of hybrid where coarser grids are tackled by algebraic multigrid while fine grids benefit from geometric multigrid with rediscrretization: our approach is hybrid as we (i) stick to the geometric multigrid structure but have algebraic operators and (ii) determine algebraic operators but store only their difference to geometric operators. The present manuscript’s idioms perform on reasonably well-posed problems. They enlarge the applicability of geometric multigrid with all its geometric advantages. This enlargement is made possible by an integration of known multigrid techniques. Their elegant integration is, to the best of our knowledge, new.

Table 1: Overview of discussed implementation techniques (first row) with references to corresponding manuscript sections (second row). Where appropriate, we add in the bottom part in which previous work we have studied related or similar concepts. Dissertations, as they have not appeared in peer-reviewed journals, are put in brackets.

Techniques:	Matrix-free on spacetree with rediscritisation and HTMG	Element-wise tree block smoothers	Galerkin and BoxMG	Operator compression	Shared memory	Distributed memory
Section	Sect. 4.1	Sect. 4.2	Sect. 4.3,4.4	Sect. 5	Sect. 6.1	Sect. 6.2
Additive	[40] without HTMG, [42]					
BPX	[42]					
Multiplicative	([54])	(([53]))	(([53]))	[12] for unknowns instead of stencils [23] for unknowns in SPH	(([53]))	(([54]),([53]))

## 2 Previous work and shortcomings of present approach

Peano [55, 57] serves as code base to realize our single-touch tree traversals. All implementation ideas however apply to other spacetree software, too. Single-touch additive multigrid solvers for spacetrees with rediscritization are subject of discussion in [40], though the discussion lacks details on the handling of dynamic adaptivity. The FAS and HTMG combination is explored in [54], and detailed for additive multigrid and BPX in [42]. A combined, concise presentation for additive, BPX and multiplicative solvers is new (cmp. Table 1).

Our augmentation of tree solvers with block smoothers stems from the dissertation [53] where block smoothers are solely applied to multiplicative solvers. The present manuscript generalizes them to additive and BPX solvers, too. (**author?**) [53] also introduces the fusion of the tree with Galerkin operators and BoxMG—again solely for the multiplicative case and lacking our mirroring/reference element idea which simplifies the coding. The compression of solution data through a hierarchical transform is explored in [12] for multigrid and in [23] for SPH codes. Its application to the operators is, to the best of our knowledge, new, though we reuse some the aforementioned mechanisms. Fragments of our shared memory or distributed memory concepts first can be found in [54] or [53], respectively. We focus on the correlation with multigrid and a theoretical concurrency analysis here, while technical details are subject of other publications [24, 55].

Our studies concentrate on operators with the sparsity pattern of d-linear discretization and inter-grid transfer operators. Wider operators, which are reasonable from an HPC point of view [26] or mandatory if stronger solver ingredients are required, induce different memory access patterns. The present ideas continue to apply but require additional work. Besides that, our experimental data stem from a multigrid prototype which is not tuned. For real-world computations, real scalability and performance engineering is mandatory, and it might turn out that it is reasonable to compromise between our academic approach and severely optimised strategies and existing libraries. Manycore vectorization for example has been successfully demonstrated [42] where we fuse our tree paradigm with batched BLAS concepts [21]. In general, performance and scalability engineering for particular problems requires tailored solutions. Finally, our experiments restrict to academic setups challenging enough to uncover the approach’s potential. It is obvious that the application to real-world experiments introduces further challenges such as more sophisticated boundary conditions.

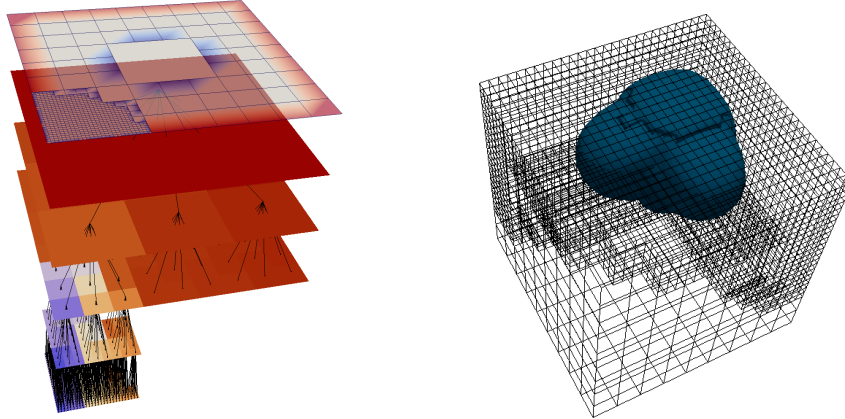


Figure 1: Left: Spacetree for  $d = 2$  from [56]. The top layer shows an adaptive Cartesian grid that results from a union of the individual levels of the tree (below). Right: Grid for the three-dimensional convection-diffusion equation in the `checkerboard` setup with an isosurface of the solution at  $u = 0.1$ .

Besides experimental and implementational limitations due to the manuscript’s scope, there are conceptual limitations to the presented family of solvers: Our approach reduces the memory footprint and data exchange but sacrifices compute power. Roadmaps predict that this is a reasonable strategy for next generation linear algebra [2]. However, the flops are not for free yet. The most severe restriction is that our approach cannot tackle problems where geometric coarsening cannot resolve coarse-scale effects (as convection) anymore or where the discretization requires very strong smoothers. As such phenomena typically arise for coarser discretizations, it will remain obligatory for these applications to apply algebraic or direct solvers on coarse levels, even though our techniques are applied. The proposed approach can widen this notion of coarseness: Our solvers remain stable for way coarser convection operators than a pure geometric approach.

### 3 Spacetrees and FAS on generating systems

Let a spacetree be a generalization of octrees or quadtrees w.r.t. the dimension  $d$  and the cut cardinality  $k \geq 2$  (Fig. 1): We embed  $\Omega$  into a  $d$ -dimensional hypercube and cut it equidistantly into  $k$  pieces along each coordinate axis. The original hypercube is the *root*. It acts as parent node to the newly created  $k^d$  smaller hypercubes that are *children* of the *root*. Root in turn is the *parent* of its children. This process is repeated recursively. Per cube we decide independently whether to refine. The construction scheme yields a spacetree. Each node of the tree graph represents one *cell*, i.e., a square ( $d = 2$ ) or cube ( $d = 3$ ). Let the *level* of a cell be the minimal number of construction steps we need to create it. Root has level 0. This usage of the term level results from a graph language.

For the present paper, we use  $k = 3$  as we base our experiments on the Peano software. We traverse the trees starting from the root which represents the coarsest grid and run through them cell by cell. Efficient storage concepts for such traversals are known (cmp. Appendix A which details

the construction and traversal of the grid and the underlying data structure).

Our present codes exploit the fact that a spacetree yields a cascade of ragged Cartesian grids, i.e. each grid level defines vertices, but each level might cover a smaller part of the domain than the next coarser one. As a result, a vertex is unique through its position in space plus its level. We distinguish three different vertex types: a vertex is *hanging* if it has less than  $2^d$  adjacent cells on the same level; a vertex is *refined* if there exists another non-hanging vertex at the same position in space on a finer level, which implies that all adjacent cells are refined further; and all other vertices are *unrefined*.

Our operators stem from a finite element discretization of (1) with  $d$ -linear shape functions. This yields  $3^d$ -point stencils on regular grids. Let each non-hanging vertex induce a shape function that spans all adjacent cells of the same level. The spacetree's shape functions then form a hierarchical generating system [30]. We combine the Full Approximation Storage (FAS) [10, 52] scheme with the hierarchical generating system and the idea of the Fast Adaptive Composite-Grid Method (FAC) [32, 39]:

1. Let a refined vertex hold the nodal value of all the vertices at the same spatial position with a higher level:  $u_\ell = Iu_{\ell+1}$  with  $I$  being the point-wise injection. We copy the  $u$  values of every vertex onto the  $u$  values of coarser vertices for each vertex pair sharing the same spatial position.
2. Let a hanging vertex's value be the  $d$ -linear interpolant from the coarser meshes.
3. Rely on the same discretization technique on every level.

Smoothers then can be read from a domain decomposition point of view, where coarser grids prescribe the values at hanging nodes while fine-grid values yield Dirichlet values in regions of the coarse grid overlapped by finer discretizations. This renders the handling of hanging nodes and, more general, adaptivity straightforward. Notably, it implies that any discretization stencil can be unaware of resolution transitions. Otherwise, the region where a fine grid transitions into a correction grid as it is refined further requires special attention and additional coding (Figure 2): The semantics of the degrees of freedom change from discretization weights into correction weights. While the degrees of freedom at the transition have to carry the solution as they act as boundary to the PDE solve on coarse mesh parts, their degree of freedom weights have to approach zero once the solution starts to converge. A FAS, i.e. a scheme that starts to change coarse grid values from an injection of fine grid solutions, removes this contradiction:  $u_\ell$  plays two different roles in adaptive meshes. In unrefined regions, it carries a discretization of the PDE, while it carries solution plus correction otherwise.  $A_\ell$  plays two roles, too. In unrefined regions, it represents a discretization of the PDE, while it encodes discretization plus correction term in refined regions. The operator does not have to be changed at resolution transitions, which otherwise yields a large number of modified stencils even if we apply tree balancing [44] to reduce the number of possibilities of coarse to fine cell configurations. While a coarsened/injected data representation is advantageous for non-linear problems, we consequently highlight a different advantage:

**Observation 1** *FAS allows us to ignore that some unknowns of one level carry a solution while others have to carry a multigrid correction, as the latter's degrees of freedom encode a correction term plus the coarsened solution. No case distinction w.r.t. the semantics of the stencil or the unknown is required.*

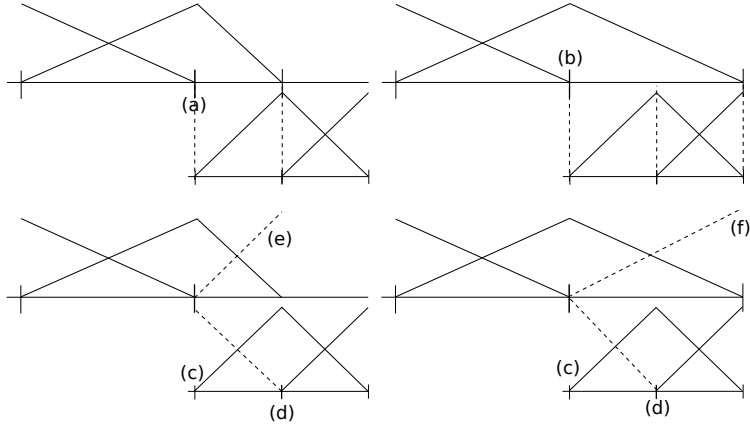


Figure 2: Classic nodal shape functions yield discretization stencils for non-equidistant grids along the resolution boundary (in point (a) of left/top sketch), even if  $\epsilon$  and  $\nu$  are invariant. We use a marginally hierarchical basis (top right) where the stencil in (b) can be computed such as any other stencil on this level. No source code modification is required. We read the adaptive grid as overlapping domain decomposition with Dirichlet-Dirichlet coupling: In both variants, the hanging node acts on the fine grid as if there were an additional shape function halve centred in (c). No stencil is to be altered w.r.t. coarse-fine transitions in point (d). The values in (e) or (f), respectively result from injection, i.e. these points can be read as halved shape functions placed on the coarse grid, acting as Dirichlet points there, and thus coupling fine grid to coarse grid solution. In a multigrid context, (f) plays two roles: it acts as coarse system Dirichlet point and as left-most correction point on the coarser level. This induces a transition dilemma: the point carries the solution while it should be zero for the exact solution, e.g. With FAS, all correction system points carry a nodal representation, too, i.e. this dilemma is resolved.

All discretization operators have strict local support, as a stencil spans  $3^d$  neighbouring vertices. Let inter-grid transfer operators have local support, too. A *parent* vertex  $b$  of a vertex  $a$  is any vertex that has at least one adjacent cell that is a parent of an adjacent cell of  $b$ . Interpolation and restriction couple vertices and parents only. The notion of parent vertices here is slightly too generous. The  $d$ -linear interpolation and restriction operators are actually even sparser.

The spacetree’s cascade of grids embeds function spaces into each other. We propose to exploit this beyond sole FAS through the HTMG idea [29]. Let  $A_\ell u_\ell = b_\ell$  be the linear equation system for (1) on a level  $\ell$ . The  $u_\ell$  here are weights of the shape functions in  $\Omega_{h,\ell}$  and comprise degrees of freedom on the fine grid mesh of level  $\ell$ . They also contain correction degrees of freedom if there are unrefined vertices on  $\ell$ . The  $b_\ell$  result from a discretization of  $f$  if we are on the finest level. Otherwise, they comprise a multigrid correction component. Instead of a correction equation, we use the Petrov-Galerkin coarse-grid operator definition, switch to FAS and solve

$$A_\ell(u_\ell + e_\ell) = R(b_{\ell+1} - A_{\ell+1}(id - PI)u_{\ell+1}) =: R(b_{\ell+1} - A_{\ell+1}\hat{u}_{\ell+1}) =: R\hat{r}_{\ell+1}.$$

Here,  $A_\ell$  is the level operator,  $e_\ell$  or  $r_\ell$  are the nodal shape function correction weights and residuals, respectively,  $P$  and  $R$  are prolongation and restriction,  $id$  is the identity,  $\hat{r}$  is called the hierarchical residual, and  $\hat{u}$  the hierarchical value. Given an injected (a coarse) representation of the solution on a level  $\ell$  through  $I$ , a multigrid solver computes a coarse-grid update, keeps track of this coarse-grid solution modification  $e_\ell$  and prolongs this value back to the fine grid later all with one set of unknowns.

Our solver family relies on the following spacetree traversal paradigm:

**Definition 1** *A multiscale element-wise traversal of the spacetree is a traversal of the cascade of grids  $\Omega_{h,\ell}$  where*

1. *each cell is processed only once, and the traversal offers throughout this processing access to all adjacent vertex data,*
2. *each cell access allows for access to the cell’s parent as well as its adjacent vertices,*
3. *and a refined cell is processed after its children.*

Def. 1 gives a partial order on the tree. The order can be formalised as a set of operation applications *handleCell*. These operation applications (*events*) are implemented as function calls that are invoked at certain points during the spacetree traversal. *handleCell* implicitly introduces two further orders *touchVertexFirstTime* and *touchVertexLastTime* on the tree’s vertices that specify when a vertex is read for the first time and for the last time. Mirroring the statements from Def. 1, the corresponding operations shall have access to their parent data, too.

We finally augment this set by a fourth transition: *descend* accepts a cell and its adjacent vertices as well as the  $3^d$  children of the cell with their vertices and precedes any *handleCell* on any child. Such an event fits into a depth first traversal and does preserve the single touch policy—every cell/vertex is read only once per multiscale grid sweep—if we make the traversal code load within a refined cell first all  $k^d$  children cells before it continues to recurse further (Figure 16 in the appendix). Traversals loading more than the direct children make some assumptions or have to have knowledge about the grid structure. *descend* does not need this and thus fits to our strictly element-wise mindset.

Definition 1 is a formalisation of our algorithmic ingredients which directly fits to many standard ways to run through a spacetree, in particular depth-first and breadth-first. Depth-first traversals of spacetrees always resemble the construction of space-filling curves as long as the run-through

Table 2: Overview of unknowns per vertex  $v$  in the three geometric multigrid variants. **pers** indicates that the value is required in-between two solver iterations, i.e. has to be stored persistently. **tmp** denotes that it is required only temporarily.

	Description	Add	BPX	Mult
$u$	Weight of shape function centred at vertex, i.e., function value in $v$ .	pers	pers	pers
$\hat{u}$	Hierarchical surplus in $v$ , i.e. difference to coarsened solution.	tmp	tmp	tmp
$r$	Residual.	tmp	tmp	tmp
$\hat{r}$	Hierarchical residual.	tmp	tmp	tmp
$d$	Helper variable transferring solver updates (deltas) between levels.	pers	pers	pers
$b$	Right-hand side.	pers	pers	pers
$i$	Injected impact of the smoother.		pers	

order of the  $k^d$  children of a parent is deterministic. Notably, Hilbert and Morton ( $k = 2$ ) and Peano ( $k = 3$ ) fall into place.

## 4 Solver realizations

A stencil of a vertex  $v$  describes the entries of one row in  $A_\ell$ . Such a row  $(A_\ell)_v$  decomposes over the cells adjacent to  $v$ . To compute  $r_v = (A_\ell)_v u$ , we can either compute  $r_v$  by a sum over the vertices, or we can split up  $(A_\ell)_v$  additively over all the cells and accumulate  $r_v$  element-wisely. For  $d = 2$ , the stencil

$$\begin{bmatrix} s_6 & s_7 & s_8 \\ s_3 & s_4 & s_5 \\ s_0 & s_1 & s_2 \end{bmatrix} \text{ decomposes into } \begin{bmatrix} s_6 & \frac{s_7}{2} & 0 \\ \frac{s_3}{2} & \frac{s_4}{4} & 0 \\ 0 & 0 & 0 \end{bmatrix} + \begin{bmatrix} 0 & \frac{s_7}{2} & s_8 \\ 0 & \frac{s_4}{4} & \frac{s_5}{2} \\ 0 & 0 & 0 \end{bmatrix} + \begin{bmatrix} 0 & 0 & 0 \\ 0 & \frac{s_4}{4} & \frac{s_5}{2} \\ 0 & \frac{s_1}{2} & s_2 \end{bmatrix} + \begin{bmatrix} 0 & 0 & 0 \\ \frac{s_3}{2} & \frac{s_4}{4} & 0 \\ s_0 & \frac{s_1}{2} & 0 \end{bmatrix}. \quad (2)$$

### 4.1 Geometric multigrid variants

The realization of a multiplicative, geometric multigrid solver within strictly element-wise space-tree traversals requires a state automaton  $S$  steering the algorithm. Let  $S$  have two properties  $current(S)$  and  $old(S)$  that identify the current smoothing level and the previous one. At startup,  $current(S) = old(S) = \ell_{max}$ . The automaton  $S$  supports two transitions: If we invoke  $S \leftarrow ascend(S)$ ,  $current(S)$  is decreased. If we invoke  $S \leftarrow descend(S)$ ,  $current(S)$  is increased.

Both operations are controlled from a loop over the multigrid iterations. Within, the actual multigrid solver is a set of nested for loops mirroring the well-known V- or W-cycle pattern. We study only  $V(\mu_{pre}, \mu_{post})$ -cycles with  $\mu_{pre} \geq 1$  and  $\mu_{post} \geq 1$  here. From within these loops, Algorithm 1 is run once per multigrid cycle step. If we realize a  $V(\mu_{pre}, \mu_{post})$ -cycle, the algorithm's recursive function is invoked  $(\mu_{pre} + \mu_{post})(\ell_{max} - \ell_{min} + 1)$  times. The  $S$  state transitions are invoked between two function calls. We end up with three different state configurations. For  $current(S) = old(S)$ , we perform either a pre- or a post-smoothing step, which is not the first smoothing step on level  $current(S)$ . For  $current(S) = old(S) - 1$ , we run the first pre-smoothing step on  $current(S)$  and restrict the right-hand side from level  $old(S)$  to the next coarser level. For  $current(S) = old(S) + 1$ , we run the first post-smoothing step on  $current(S)$  and prolong corrections from level  $old(S)$  to the next finer level.

Cells contribute to the residual either if they are on the active level or if they belong to a level that is coarser than the active level and are adjacent to at least one unrefined vertex. Such a

---

**Algorithm 1** Geometric multiplicative multigrid with rediscrretization. It embeds into a multiscale element-wise spacetree traversal such as a depth-first ordering and is invoked by  $\text{GEOMMULT}(\ell_{max}, S)$  per smoothing step.  $S$  is a state machine holding the current and previous active smoothing level. The combination of these two levels distinguishes pre- from post-processing and triggers inter-grid data transfers.

---

```

1: function GEOMMULT( $\ell, S$ )
2:   if  $\ell = \text{current}(S) \vee (\text{current}(S) > \ell \wedge \text{vertex unrefined})$  then  $r_\ell \leftarrow 0$  end if
3:   if  $\ell = \text{current}(S) \vee (\text{current}(S) > \ell \wedge \text{vertex unrefined})$  then  $\hat{r}_\ell \leftarrow 0$  end if
4:   if  $\text{current}(S) < \text{old}(S) \wedge \text{old}(S) = \ell$  then  $\hat{u}_\ell \leftarrow u_\ell - Pu_{\ell-1}$  end if
5:   if  $\text{current}(S) < \text{old}(S) \wedge \text{current}(S) = \ell \wedge \text{vertex refined}$  then  $b_\ell \leftarrow 0$  end if
6:   if  $\text{current}(S) > \text{old}(S) \wedge \text{current}(S) = \ell$  then  $u_\ell \leftarrow u_\ell + Pd_{\ell-1}$  end if
7:   if  $\text{current}(S) > \text{old}(S) \wedge \text{current}(S) = \ell$  then  $d_\ell \leftarrow d_\ell + Pd_{\ell-1}$  end if
8:   if  $\ell < \ell_{max} \wedge \ell < \max\{\text{current}(S), \text{old}(S)\}$  then GEOMMULT( $\ell + 1, S$ ) end if
9:   if  $\text{current}(S) = \ell \vee \text{current}(S) < \ell \wedge \text{cell unrefined}$  then  $r_\ell \leftarrow -A_\ell u_\ell$  end if
10:  if  $\text{current}(S) < \text{old}(S) \wedge \ell = \text{old}(S)$  then  $\hat{r}_\ell \leftarrow -A_\ell \hat{u}_\ell$  end if
11:  if  $\text{current}(S) = \ell \vee \text{current}(S) < \ell$  then  $r_\ell \leftarrow r_\ell + b_\ell$  end if
12:  if  $\text{current}(S) < \text{old}(S) \wedge \ell = \text{old}(S)$  then  $\hat{r}_\ell \leftarrow \hat{r}_\ell + b_\ell$  end if
13:  if  $\ell = \text{current}(S) \vee (\text{current}(S) > \ell \wedge \text{vertex unrefined})$  then
14:     $u_\ell \leftarrow u_\ell + \omega \text{diag}^{-1}(A_\ell) r_\ell$  end if
15:   $d_\ell \leftarrow \begin{cases} 0 & \text{if } \ell = \text{current}(S) \wedge \text{vertex refined} \\ d_\ell + \omega \text{diag}^{-1}(A_\ell) r_\ell & \text{if } \ell = \text{current}(S) \vee (\text{current}(S) > \ell \wedge \\ & \text{vertex unrefined}) \\ d_\ell & \text{otherwise} \end{cases}$ 
16:  if  $\text{current}(S) \geq \ell$  then  $u_{\ell-1} \leftarrow Iu_\ell$  end if
17:  if  $\text{current}(S) < \text{old}(S) \wedge \text{old}(S) = \ell$  then  $b_{\ell-1} \leftarrow R\hat{r}_\ell$  end if
18: end function

```

---

multiscale smoothing can be read in a domain decomposition way, where coarse-grid values are overwritten by overlapping fine-grid values. Many multiplicative multigrid codes coarsen all grid regions when they ascend. The present code, in contrast, coarsens the levels that are finer than the previous smoothing level. This makes the code easier to understand. A fine-grid region then is subject to the more smoothing steps the coarser it is.

**Observation 2** *We can implement matrix-free, geometric multiplicative multigrid within an element-wise multiscale traversal with one smoothing step per grid sweep.*

In [42], two additive solver alternatives are presented that work in an element-wise multiscale traversal and both require, amortized, one multiscale grid sweep per additive cycle. The versions of these solvers that we use in this work are Algorithm 2 and Algorithm 3. Algorithm 2 is a classical additive scheme, and Algorithm 3 is a BPX variant. A detailed description these algorithms and their implementation can be found in Appendix B.

**Observation 3** *We can implement a matrix-free, geometric additive multigrid solver (a solver based upon  $d$ -linear inter-grid operators and rediscrretization of coarse grid matrices) within an element-wise multiscale traversal that requires, amortized, one multiscale grid sweep per additive cycle.*

**Observation 4** *We can implement a matrix-free, geometric BPX solver within an element-wise multiscale traversal that requires, amortized, one multiscale grid sweep per additive cycle.*

**Algorithm 2** Geometric additive multigrid based upon rediscrretization. It embeds into a multiscale element-wise spacetime traversal such as a depth-first ordering and is invoked by  $\text{GEOMADD}(\ell_{max})$ . If all hanging nodes are made to hold the  $d$ -linear interpolant of the next coarser levels, the code works on arbitrary adaptive meshes.

---

```

1: function GEOMADD( $\ell$ )
2:    $d_\ell \leftarrow d_\ell + Pd_{\ell-1}$ ;  $u_\ell \leftarrow u_\ell + Pd_{\ell-1}$ ;  $\hat{u}_\ell \leftarrow u_\ell - Pu_{\ell-1}$  ▷ Vertex-wise correction
3:    $r_\ell \leftarrow 0$ ;  $\hat{r}_\ell \leftarrow 0$  ▷ (coarse-to-fine data flow)
4:    $b_\ell \leftarrow 0$  for all  $b$  associated to refined vertices
5:   if  $\ell < \ell_{max}$  then GEOMADD( $\ell + 1$ ) end if ▷ Recursion into finer grid levels
6:    $r_\ell \leftarrow -A_\ell u_\ell$ ;  $\hat{r}_\ell \leftarrow -A_\ell \hat{u}_\ell$  ▷ Cell-wise residual accumulations
7:    $r_\ell \leftarrow r_\ell + b_\ell$ ;  $\hat{r}_\ell \leftarrow \hat{r}_\ell + b_\ell$ 
8:    $d_\ell \leftarrow \omega \text{diag}^{-1}(A_\ell) r_\ell$  ▷ Vertex-wise smoothing
9:    $u_\ell \leftarrow u_\ell + d_\ell$ 
10:  if  $\ell > \ell_{min}$  then  $u_{\ell-1} \leftarrow Iu_\ell$ ;  $b_{\ell-1} \leftarrow R\hat{r}_\ell$  end if ▷ Vertex-wise restriction and injection
11: end function

```

---

**Algorithm 3** Geometric BPX variant with rediscrretization. It embeds into a multiscale element-wise spacetime traversal such as a depth-first ordering and is invoked by  $\text{GEOMBPX}(\ell_{max})$ .

---

```

1: function GEOMBPX( $\ell$ )
2:    $d_\ell \leftarrow d_\ell + \begin{cases} Pd_{\ell-1} & \text{if c-point} \\ Pd_{\ell-1} - Pi_{\ell-1} & \text{else} \end{cases}$  ▷ Vertex-wise operations from GEOMADD
3:    $u_\ell \leftarrow u_\ell + \begin{cases} Pd_{\ell-1} & \text{if c-point} \\ Pd_{\ell-1} - Pi_{\ell-1} & \text{else} \end{cases}$  ▷ with modified prolongation
4:    $\hat{u}_\ell \leftarrow u_\ell - Pd_{\ell-1}$ 
5:    $r_\ell \leftarrow 0$ ;  $\hat{r}_\ell \leftarrow 0$ 
6:    $b_\ell \leftarrow 0$  for all  $b$  associated to refined vertices
7:   if  $\ell < \ell_{max}$  then GEOMBPX( $\ell + 1$ ) end if
8:    $r_\ell \leftarrow -A_\ell u_\ell$ ;  $\hat{r}_\ell \leftarrow -A_\ell \hat{u}_\ell$ 
9:    $r_\ell \leftarrow r_\ell + b_\ell$ ;  $\hat{r}_\ell \leftarrow \hat{r}_\ell + b_\ell$ 
10:   $d_\ell \leftarrow \omega \text{diag}^{-1}(A_\ell) r_\ell$ 
11:   $u_\ell \leftarrow u_\ell + d_\ell$  for non-c-points
12:  if  $\ell > \ell_{min}$  then  $b_{\ell-1} \leftarrow R\hat{r}_\ell$ ;  $i_{\ell-1} \leftarrow Id_\ell$  end if ▷ Injection of skipped updates
13:   $d \leftarrow 0$  for c-points ▷ Skip update
14: end function

```

---

## 4.2 Spacetime block smoothers

Strict element-wise matvecs that touch each (fine-grid) cell only once render smoothers beyond point Jacobi technically challenging if a whole smoothing step has to be realized within one grid traversal. We can update an unknown only once a vertex is used for the last time (in (2) once the fourth cell has been processed), and information of a vertex update thus can propagate only along the grid traversal sequence: A vertex update may only affect vertices that are adjacent to the last cell processed that is adjacent to this vertex. We observe that a naive splitting of a stencil into equal parts as realised in (2) then is not possible anymore and the splitting has to anticipate the Gauss-Seidel like enumeration.

Gauß-Seidel with an unknown enumeration that is not tied to the cell traversal order or line smoothers can not be realized within one grid traversal. Coloured schemes such as red-black Gauss-Seidel require one grid traversal per colour. Krylov schemes work if we evaluate the matvec as well as all scalar products in one grid sweep and apply the impact in a second sweep [5]. With pipelining, multiple sweeps can be fused and the amortized cost per unknown update can be reduced [26]. In the present work, we however restrict ourselves to multigrid ingredients with minimalist memory

access and thus stick to Jacobi.

Point Jacobi is a poor choice for many non-trivial parameter combinations in (1). To facilitate more powerful smoothers without giving up data locality or single touch, we augment Jacobi by an additional block smoothing that improves convergence locally on very small subdomains ( $k^d$  patches). For this, we generalize the tree traversal by a *descend* event (see Sect. 3). In a depth-first traversal code, such an operation makes a recursive step down within the tree and loads all children of a node before it continues recursively—a one-level recursion unrolling [24].

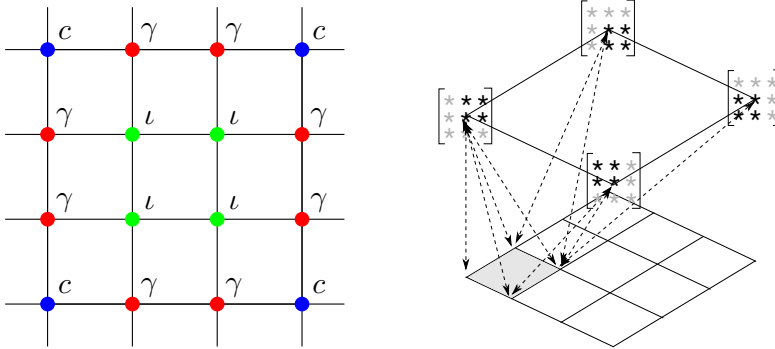


Figure 3: Left:  $3^d$  patch available to *descend* (together with the parent cell). We distinguish three vertex types:  $c$ -points coincide with vertices on the next coarser grid level,  $\gamma$ -points lie on coarse-grid lines, and  $\iota$ -points lie within the patch. Right: Illustration of a cell-wise Galerkin coarse grid operator computation. With  $P$  and  $R$  known, we can set the interpolation for the vertices of a cell, apply the element matrix and add the result back to the coarse cell’s stencils via  $R$ . Coarse-grid stencil entries subject to accumulation are bold.

A block smoother accepts all  $(k + 1)^d$  vertices and runs the solver’s correction steps for them if not triggered by adjacent cells already. We distinguish three different types of vertices (Fig. 3)—the nomenclature follows the BoxMG terminology as detailed in Sect. 4.4—and we use the term *block Jacobi* for a smoother that performs Jacobi on the  $\gamma$  and  $c$  points and processes the  $\iota$  vertices differently. When block Jacobi loads a patch’s  $(k - 1)^d$   $\iota$ -vertices for modification (clearance of right-hand sides, e.g.) it first runs Gauß-Seidel sweeps on them. Then it computes the respective operations from the algorithm, determines the hierarchical surplus and continues in an element-wise fashion.

While an exact solve on the interior points of a patch would be possible and even trivial for  $k = 2$ , we use  $k = 3$  and find it convenient to make the patch sweeps run Gauß-Seidel iterations. For the geometric multigrid solver, these iterations use on-the-fly rediscrretization. For the Galerkin coarse grid variants using  $d$ -linear or BoxMG inter-grid transfer operators we make them use stencils that are explicitly available. The proposed technique falls into the class of hybrid smoothers [6].

**Observation 5** *Through an augmentation of the multiscale element-wise spacetree traversal with a descend operation, the realization of block Jacobi smoothers is straightforward. They preserve the data locality of the element-wise traversal.*

### 4.3 Galerkin multigrid variants

Galerkin in our tests denotes all multigrid variants where prolongation and restriction are  $d$ -linear, while coarse grid operators result from  $A_{\ell-1} = RA_\ell P$ . The Galerkin computation rules do not imply any assumption about  $P$  and  $R$ . As a computation of  $A_{\ell-1}$  depends on a cascade of evaluations on finer levels, an on-the-fly computation of  $A_{\ell-1}$  is impossible. The coarse-grid system has to be held explicitly. For this, we augment the vertex records with  $3^d$  (for multiplicative multigrid) or  $2 \cdot 3^d$  (for additive and BPX) doubles. They hold the stencil associated with a vertex that in turn determines the element-wise matrices. All  $r \leftarrow -A_\ell u$  and  $\hat{r} \leftarrow -A_\ell \hat{u}$  evaluations are modified such that they read the stencils from the cells' adjacent vertices. Whenever we create a new vertex, the stencil entries are initialized via PDE discretization. To determine the Galerkin operator, we accumulate the coarse-grid operator element-wisely together with the residual by decomposing  $A_{\ell-1}|_v = (RA_\ell P)|_v$  over all  $2^d \cdot 3^d$  child cells  $\hat{c}$  of the cells adjacent to  $v$  (Fig. 3, right). This strategy is element-wise w.r.t. level  $\ell - 1$ .

To make the accumulation work, we have to clear the stencils before. If a grid is stationary and the PDE is linear, we could skip any re-accumulation of coarse-grid operators. If the grid however refines into a level  $\ell + 1$ , fine grid stencils on a level  $\ell$  that are associated to newly refined vertices transform into stencils that carry a Galerkin operator and thus have to be recomputed. This re-computation recursively triggers stencil updates on coarser levels. If the PDE is non-linear, the stencils on the finest level depend on the current approximate solution  $u_h$  and thus trigger changes recursively on all coarser levels as soon as we update  $u_h$ . Even if we stick to linear problems such as (1), it is convenient to recompute the coarse-grid operators in every cycle before we coarsen in the spacetime. We then do not have to analyze whether the grid changes. Our vertical integration of multigrid operations suggests that all fine-grid operators influencing a Galerkin recomputation are held in caches. The re-accumulation does not increase the pressure on the memory subsystem. Finally, we could omit the storage of the stencils on the finest grids and rely on on-the-fly discretization. Yet, we introduce a holistic memory compression applying to all grid levels in Sect. 5 that realises this storage optimisation automatically.

If we recompute the Galerkin operator in each traversal, we need both a valid operator and memory to accumulate the coarse grid stencils for the additive solver variants. Additive multigrid and the BPX variant thus store a copy of the stencil upon the first read of a vertex in the data structure. Hereafter, all current stencil entries are cleared and we start the accumulation. Matvecs use the backup copy, which can be held temporarily, i.e., not stored in-between two grid sweeps. A Galerkin variant of the multiplicative Algorithm 1 does not require duplicated stencils. Let

$$\text{recomputeGalerkin}(\ell, S) = \begin{cases} \top & \text{if } \ell + 1 = \text{current}(S) \wedge \text{last smoothing step} \\ & \text{on level } \ell + 1 \wedge \text{vertex refined} \\ \perp & \text{otherwise.} \end{cases} \quad (3)$$

A vertex's stencil is set to zero when we read the vertex for the first time if  $\text{recomputeGalerkin} = \top$ . Coarse operator contributions are added to those coarser vertices where the predicate holds. They are not altered on finer grids than the active smoothing level or during the descend process.

**Observation 6** *If we augment each vertex data structure by  $3^d$  (multiplicative) or  $2 \cdot 3^d$  (additive and BPX) doubles, we can realize Galerkin multigrid variants within the element-wise multiscale traversal that work on-the-fly.*

A proper choice of  $\ell_{max}$  is delicate for multigrid methods: If  $\ell_{max}$  is too fine, multigrid convergence suffers. If  $\ell_{max}$  is too coarse, the Galerkin operators deteriorate, might become indefinite, and, in

the worst case, the coarse grid smoothing contributions destroy the overall convergence and make the solver diverge [61]. We propose to rely on a dynamic coarsest level which starts with  $\ell_{max} = 1$ . On the one hand, the solver increases  $\ell_{max}$  in-between two multigrid cycles/iterations once we observe stagnating or growing residuals. On the other hand, the solver immediately increases  $\ell_{max}$  if one Galerkin operator computation yields a coarse grid stencil that is not diagonal dominant anymore or carries negative diagonal values. This approach makes our solver variants start as a multilevel approach and deteriorate, in the worst case, to (block) Jacobi. We note that the definiteness check is, in principle, active only at the solver startup, if the underlying PDE is linear. The convergence speed criterion however can kick in later. For more sophisticated applications, it might be reasonable to make  $\ell_{max}$  space-dependent, too. We do not follow-up such a sophisticated scheme.

## 4.4 BoxMG

To construct PDE-dependent inter-grid transfer operators, we rely on BoxMG [16] applied to tri-partitioning [20, 53, 61]. It has been shown to yield robust and efficient multigrid solvers for a large class of problems while it can be seen as a special case of classical algebraic multigrid with a geometric definition of “strong connections” [36]. It thus fits to our geometric multiscale meshing concept. For studies on the robustness and efficiency of BoxMG, we refer to [17, 19, 41], and notably cite [59] offering a framework for the construction of prolongation operators where BoxMG is recovered as a special case of more general multigrid techniques.

For any refined vertex, this vertex’s inter-grid transfer operator affects  $5^d$  fine grid vertices. It carries a  $5^d$  stencil for  $P$  and  $R$ . Instead of discussing how the inter-grid stencils affect the  $5^d$  fine grid vertices, we

- clear  $P$  and  $R$  upon a coarse grid vertex load,
- plug into *descend* when we descend from an refined cell that is adjacent to the vertex into the finer grids,
- collect there the  $4^d$  stencils from the fine grid vertices, and
- alter the  $3^d$  affected stencil entries of the coarse grid,

whenever these are to be recomputed. In exchange, *descend* always computes  $2^d$  partial inter-grid transfer stencils per cell, i.e. contributes to the stencils of all the vertices adjacent to a cell. We fit to the concept of element-wise assembly for the multigrid.

As we work with cubes only, any vertex/stencil configuration can be mirrored by a matrix  $M$  such that the coarse vertex and its stencil of interest coincide with the left, bottom vertex.  $M$  reorders the vertices within a  $3^d$  patch and all of their stencils, too. Once we have determined all  $P$  entries of interest— $R$  follows due to  $R^T = P$  if not explicitly stated otherwise—we can mirror all entries back through  $M^T$ . We break down BoxMG into multiscale element-wise operations that we formalise w.r.t. one vertex configurations from which  $2^d - 1$  further operations results through mirroring.

Our presentation restricts to one partial inter-grid transfer stencil therefore. Following the literature, we distinguish  $c$ -,  $\gamma$ - and  $\iota$ -points (Fig. 3) within a  $3^d$  patch and re-order the equation system accordingly. All formalism and techniques are here described for  $d = 2$  and extend naturally

to the three-dimensional case. For the complete operators, we refer to Appendix C. Let the stencil  $P$  be equivalent to the vector  $P = (P_c P_\gamma P_\iota)^T$ . In  $2d$ , the entries read

$$P = \begin{bmatrix} p_{0,4} & p_{1,4} & p_{2,4} & p_{3,4} & p_{4,4} \\ p_{0,3} & p_{1,3} & p_{2,3} & p_{3,3} & p_{4,3} \\ p_{0,2} & p_{1,2} & p_{2,2} & p_{3,2} & p_{4,2} \\ p_{0,1} & p_{1,1} & p_{2,1} & p_{3,1} & p_{4,1} \\ p_{0,0} & p_{1,0} & p_{2,0} & p_{3,0} & p_{4,0} \end{bmatrix} \mapsto \underbrace{(p_{2,2})}_{P_c}, \underbrace{(p_{3,2}, p_{4,2}, p_{2,3}, p_{2,4})}_{P_\gamma}, \underbrace{(p_{3,3}, p_{4,3}, p_{3,4}, p_{4,4})}_{P_\iota}^T$$

with lexicographic stencil entry enumeration for the prolongation stencil associated to the bottom left coarse grid vertex of a  $3 \times 3$  patch (Fig. 3). BoxMG makes the impact of a coarse-grid correction  $u_{\ell-1}$  onto  $u_\ell$  fall into the PDE's nullspace. Its operator-dependent inter-grid transfer implies that an interpolation of coarse data fits to the PDE.

$$A_\ell P u_{\ell-1} = \begin{pmatrix} A_{cc} & A_{c\gamma} & A_{c\iota} \\ A_{\gamma c} & A_{\gamma\gamma} & A_{\gamma\iota} \\ A_{\iota c} & A_{\iota\gamma} & A_{\iota\iota} \end{pmatrix} \begin{pmatrix} P_c \\ P_\gamma \\ P_\iota \end{pmatrix} u_{\ell-1} = \begin{pmatrix} b_c \\ b_\gamma \\ b_\iota \end{pmatrix}, \quad (4)$$

$p_{2,2}=1$  induces  $5^d - 1$  interpolated fine grid values that disappear under the PDE operator. To achieve this,  $P = (P_c P_\gamma P_\iota)^T$  is constructed in five steps:

1. c-points are assigned the value of their coarse counterpart coinciding spatially.  $P_c = I^T$  with  $I$  from FAS.
2. We ignore the impact of  $\gamma$ - and  $\iota$ -points on c-points and from  $\iota$ -points on  $\gamma$ -points.  $A_{c\gamma} = A_{c\iota} = A_{\gamma\iota} = 0$  and, therefore,  $A_{cc} = id$ . We bring  $A_{\gamma c}$  and  $A_{\iota c}$  to the right-hand side and obtain

$$\begin{pmatrix} A_{\gamma\gamma} & 0 \\ A_{\iota\gamma} & A_{\iota\iota} \end{pmatrix} \begin{pmatrix} P_\gamma u_{\ell-1} \\ P_\iota u_{\ell-1} \end{pmatrix} = \begin{pmatrix} b_\gamma - A_{\gamma c} P_c u_{\ell-1} \\ b_\iota - A_{\iota c} P_c u_{\ell-1} \end{pmatrix}.$$

3. This system remains hard to solve as the matrices are large. BoxMG therefore decomposes the level  $\ell$  into patches (Fig. 3). To reduce inter-patch dependencies, the two-dimensional stencils belonging to  $\gamma$  points are collapsed to one-dimensional stencils by summing up all stencil entries in the dimension perpendicular to the corresponding coarse grid line. In  $d = 2$  and for coarsening by a factor of three, each two  $\gamma$  points on a coarse-grid line can be computed from the two neighbouring  $c$  points and themselves by solving two equations in two unknowns:

$$P_\gamma u_{\ell-1} = \tilde{A}_{\gamma\gamma}^{-1} (b_\gamma - \tilde{A}_{\gamma c} P_c u_{\ell-1}).$$

4. As multigrid is defined over residual equations, it is reasonable to assume  $b_\gamma = b_\iota = 0$ . This yields a linear equation for  $P_\gamma$ . More efficient BoxMG variants apply a postsmoothing step similar to smoothed aggregation to  $P$  and do not neglect the right-hand side in (4) [36]. We do not follow-up this technique though our software base in principle allows for nonhomogeneous right-hand sides.
5. Finally, the four  $\iota$  points are computed by solving four equations in four unknowns.

**Observation 7** *BoxMG yields operator-dependent inter-grid transfer operators that can be represented by  $5^d$ -stencils per vertex. We thus can realize an algebraic-geometric multigrid solver without any external global matrix if we store these stencils within the vertices.*

The extension of the scheme to three dimensions is straightforward [9, 18, 46, 61]: The stencils are collapsed into  $1d$  stencils along patch cube edges and into  $2d$  stencils on the patch faces. An  $8 \times 8$  equation system is to be solved in the patch interior. We summarise the key property of BoxMG’s construction from a traversal’s point of view: Whenever the tree traversal descends within a refined cell, it alters exactly  $3^d$  entries of any  $P$  stencil of any adjacent coarse stencil. For this, it has to know the  $3^d$  stencils of the fine grid vertices affected. Within a patch however no  $P$  entry depends on any stencil of any vertex that is not contained within the same patch.

**Observation 8** *We can implement BoxMG in a strict multiscale element-wise sense through the introduction of descend. All inter-grid transfer operators of one level become available within one grid sweep. We propose a single-sweep, single-touch inter-grid transfer operator computation.*

One advantage of additive multigrid variants is the possibility to merge coarse grid operator computations with the smoothing process ([3] and references therein). Our approach offers this property also for the multiplicative variant: Coarse-grid operator computation, level  $\ell - 1$  smoothing and restriction from level  $\ell + 1$  all are interwoven.

Plugging a symmetrized system operator  $A_{sym} = \frac{1}{2}(A_\ell + A_\ell^T)$  into the computation of either restriction or prolongation computation in the BoxMG scheme improves the convergence and robustness for non-symmetric setups [17, 61]. Such a Petrov-Galerkin multigrid scheme however changes the memory access pattern for  $P$ : As “half of  $A_{sym}$ ” stems from  $A_\ell^T$ , a patch’s computation of  $P$  entries needs the stencils of vertices surrounding a patch. It effectively uses a patch with  $5^d$  cells, i.e.  $6^d$  vertices per linear equation system solve. It currently is unclear whether we can avoid a spreading of the influence area and stick to a strictly patch-wise, localized data evaluation pattern and, at the same time, use a symmetrized operator. This has to be subject of future studies. Yet, we can use simpler symmetric restriction operators  $R$  in combination with the BoxMG prolongation  $P$ . Notably, simple injection  $R = I$  [29] or aggregation of  $5^d$  fine grid points into one coarse grid point are trivial to implement. The resulting inter-grid operator combination then lacks the accuracy required by multigrid efficiency proofs, but we know that the resulting Galerkin coarse grid operators tend to remain more stable—they do not degenerate that fast into central differences for convection-dominated flows when we coarsen [60]. We thus can expect that our adaptive coarse grid selection does not increase  $\ell_{max}$  as fast as for traditional BoxMG.

The computation of  $P$  and  $R$  fits to *descend*, and we can store the results as stencils in the vertices. Again, we need (temporary) backups of the inter-grid operators in the additive variants. All statements and details on (re-)accumulation of stencils for the coarse-grid operators apply to the BoxMG-operators, too.

The patch-based locality makes BoxMG well-suited for spacetime-based non-uniform grids. The interpolant on hanging vertices is no longer determined geometrically. It instead results from  $P$  and  $R$  according to the BoxMG formalism. At the hanging vertices, well-suited stencils that can be collapsed are required. We use  $d$ -linear interpolation of the parent stencils to obtain them. The elimination of dependencies through stencil collapsing along patches preserves the high memory access locality of an augmented element-wise multiscale traversal.

## 5 Stencil compression

Our Galerkin and BoxMG multigrid variants are not literally matrix-free. They do not hold a dedicated matrix data structure, but they store the stencils within the grid. Since sparse matrix

storage formats exist that introduce a small administrative overhead [34], the savings through this in-situ storage are limited. Yet, significant savings can be made if we omit storage on the finest grid levels and recompute the stencils there on-the-fly. This does not introduce any savings on coarser grids. If the discretization is costly—through material parameters  $\epsilon$  that have to be integrated or challenging boundary conditions, for example—it might be better for performance-wisely to store the stencils on the finest grid level, too.

Galerkin coarse-grid operators resemble rediscrretizations for smooth  $\epsilon$ , small  $v = 0$  or fine mesh sizes. We thus introduce hierarchical operators

$$\hat{A} = A - A_{\text{rediscrretized}}, \quad \hat{P} = P - P_{d\text{-linear}} \quad \text{and} \quad \hat{R} = R - R_{d\text{-linear}}.$$

$\hat{A}$ ,  $\hat{P}$  and  $\hat{R}$  can be computed whenever we use a vertex for the last time throughout a grid traversal. Either  $A$  or  $\hat{A}$  have to be held in-between two iterations, i.e., we can either store the original operator or reconstruct it from the hierarchical representation upon the subsequent vertex load. The argument holds for  $\hat{P}$  and  $\hat{R}$  analogously.

**Observation 9** *For setups where  $\epsilon$  is smooth and  $v$  is small in most of the domain, the entries of the hierarchical operators  $\hat{A}$ ,  $\hat{P}$  and  $\hat{R}$  are small. They hold fewer valid digits than made available through the IEEE standard.*

For an almost matrix-free multigrid realization, we thus propose to rewrite all three operators held within the vertex into their hierarchical representation. If the operators are zero, i.e., the stencil equals rediscrretization and the inter-grid transfer operators are  $d$ -linear we mark the vertex and discard the operator’s stencil. Otherwise, we convert all entries  $x$  of the hierarchical representation into a format  $f_{bpa}^{-1}(x) = m \cdot 2^e$ , where the exponent  $e$  is stored in one byte (C data type `char`) and  $m \in \mathbf{N}_0$ , with  $e$  chosen such that  $m$  fits exactly into  $bpa - 1$  bytes as a natural number. Here,  $bpa \in \{0, 2, \dots, 8\}$  (bytes per attribute) is the number of bytes that we use to store the exponent  $e$  plus the integer value  $m$ . Upon a vertex store, we determine per operator the smallest  $bpa$  such that  $|f_{bpa}(\hat{x}) - \hat{x}| \leq \epsilon_{mf}$  with  $\epsilon_{mf} \ll 1$ .

Within the vertex, solely  $bpa$  per stencil is held in-between two iterations. All three  $bpa$  values for  $A$ ,  $P$  and  $R$  fit into 9 bits. The values  $e$  and  $m$  per stencil entry are piped into a separate byte stream. When we read the vertex for the first time, we take  $bpa$  from the vertex record, apply  $f_{bpa}$ , add  $A_{\text{discrretized}}$  or  $P_{d\text{-linear}}$  respectively, and from hereon continue to work with the standard IEEE precision.

Such a conversion computationally is not for free but reduces the memory footprint. First, few vertices with an uncompressed operator representation are required simultaneously at the same time. Those vertices which have not been used yet or where all adjacent cells have been processed already can be held in compressed form. Second, all stencils on fine-grid vertices are removed completely from the persistent data structures as  $\epsilon$  and  $v$  here are simple. Third, all Galerkin and BoxMG inter-grid transfer operators are held persistently. Yet, their hierarchical surplus often is very small, yields small  $bpa$  and thus is compressed aggressively. The coarser the grid, the more bytes have to be invested in operator storage. This is not problematic as the number of coarser grid vertices is small.

**Observation 10** *Our implementation is almost matrix-free in terms of storage.*

Our fine grid statement is invalid if  $\epsilon$  and  $v$  on the fine grid are homogenized from subgrid sampling. Homogenized stencils differ from rediscrretization though we may expect again that the difference

is small. We also note that our approach is orthogonal to [23] and [12] where we use a hierarchical transform to reduce the memory footprint of unknowns or hierarchical surpluses, respectively. In the present approach, the unknown per vertex is only one double compared to  $2 \cdot 5^d + 3^d$  (multiplicative) or  $4 \cdot 5^d + 2 \cdot 3^d$  (additive/BPX) doubles required to store the stencils. A *bpa*-based compression of  $u$  (and probably  $b$ ) on top of the stencil compression thus would only have a minor impact.

## 6 Parallelization

Our parallelization considerations focus on shared memory and distributed memory via tasking or MPI, respectively. We rely on static load balancing and task stealing only. That is, we concentrate on an academic discussion of potential concurrency in the linear algebra and postpone performance engineering.

### 6.1 Shared memory

The dynamic adaptivity plus vertical integration render standard loop-based shared memory parallelization problematic, as we do not assume that there are larger regular grid region [24]. There are no major loops well-suited for a `parallel for` and tiling [3]. We therefore derive a task-based parallelism formalized via operation dependencies on the element-wise traversal. These dependencies can be resolved by a directed acyclic graph and then directly can be passed to any task-based library.

For all solver variants, first accesses to vertices may run in parallel as long as the traversal preserves a top-down ordering for *touchVertexFirstTime*. As soon as a set of vertices on level  $\ell$  is loaded, all vertices on level  $\ell + 1$  that share only the level  $\ell$  vertices as parents can be handled in parallel. On one level, *touchVertexFirstTime* (and thus prolongation) is embarrassingly parallel, with read-only access to the coarser level.

The element-wise residual computation exhibits a lower level of concurrency. For purely geometric multigrid solvers, no two cells may be updated concurrently that share a vertex. This induces a red-black type colouring of the cells with  $2^d$  colours. Galerkin and BoxMG solvers are more restrictive as they compute the residual and modify the coarse-grid stencil and the inter-grid transfer operators (Fig. 4). Here, two cells on level  $\ell$  may be updated in parallel if their parent cells on level  $\ell - 1$  do not share any common adjacent vertex. If we read  $\ell$  as a regular grid, this is a  $(2k)^d$  colouring of the cells. Such a multiscale dependency reduces the algorithm's concurrency severely. However, we can work with  $k^d$  colouring where possible and only use  $(2k)^d$  colours while *recomputeGalerkin* in (3) holds.

*touchVertexLastTime* updates the unknowns, restricts right-hand sides and injects data. Updates are embarrassingly parallel. As each vertex on level  $\ell$  coincides spatially with at most one vertex on level  $\ell + 1$ , the injection of vertices on level  $\ell + 1$  is embarrassingly parallel too. Again, the multiscale traversal synchronizes the individual levels and ensures that all vertices on level  $\ell$  receive a *touchVertexLastTime* before any of their shared parents is handed over to this event. The restriction imposes additional constraints. Where the interpolation reads coarse-grid data only, the restriction reads fine-grid data (modified by the update) and writes to the coarse grid. No two vertices on level  $\ell + 1$  that share a parent may thus be updated concurrently. If we read level  $\ell + 1$  as a regular grid, this implies a  $(2k + 1)^d$  colouring of the vertices. We were not able to obtain reasonable speedups if we always stucked to  $(2k + 1)^d$  colouring. Therefore, we apply this colouring

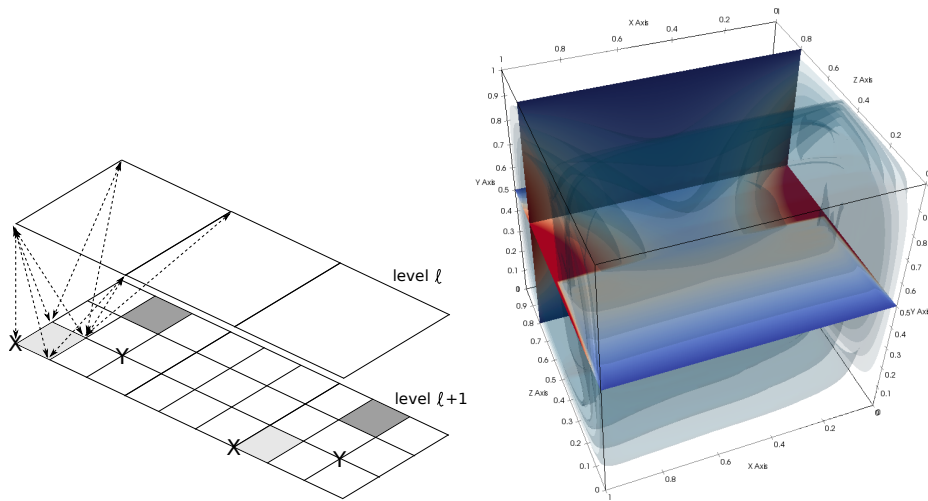


Figure 4: Left: BoxMG concurrency within the spacetime. Cells of same grey shade can be processed in parallel. All vertices can be updated in parallel upon their very first usage. Those vertices carrying an X or Y marker, e.g., can be processed in parallel when the last operations per vertex per traversal are executed. Right: Solution to the `circle` benchmark for  $d = 3$  with some contour faces. Diffusion dominates in the back half of the setup while  $\epsilon = 10^{-4}$  in the front half allows the convection to yield an asymmetric solution.

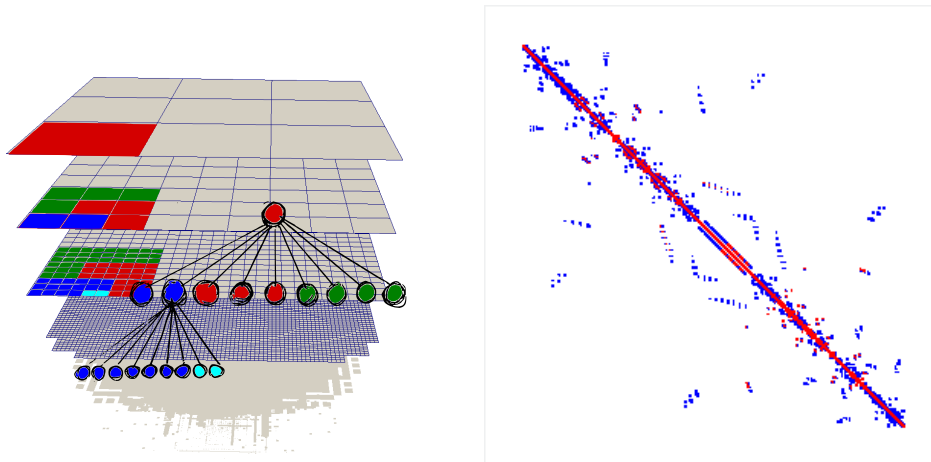


Figure 5: Left: Domain decomposition along an SFC with four ranks highlighted. The decomposition induces a logical tree topology with masters and workers among the MPI ranks (from [55]). Right: Sparsity pattern of an explicitly assembled (PETSc) matrix for the  $d = 2$  setup on regular grids. As we use a space-filling curve to traverse the finest grid, the matrix pattern is not dominated by diagonals.

only for levels and grid regions where the right-hand side needs to be re-determined. Otherwise, we process vertices embarrassingly parallel.

The *descend* events require a  $2^d$  colouring on the coarser level  $\ell$  if  $P$  and  $R$  are re-computed. Theoretically, all BoxMG patches can be computed in parallel. Yet, along the interface of two patches all adjacent patches compute the same entries due to the stencil collapsing. Though this is a race condition where multiple threads determine the same data and write the same entries, a concurrent, redundant computation of some stencil entries without a synchronization led invalid stencil entries in our implementation. We thus fall back to  $2^d$  (coarse cell) colouring where no two adjacent  $3^d$  patches determine BoxMG operators. For the block smoothers, we run the patches parallel without locks. They never modify any data on level  $\ell + 1$  (Fig. 3).

## 6.2 Distributed memory

The MPI parallelization of multigrid is an active area of research. There are dozens of different strategies for any combination of solver variant, machine and problem. In line with the shared memory parallelization, we conduct a basic data flow analysis for the multiplicative algorithms on non-overlapping multiscale decompositions here.

A decomposition scheme fitting to our notion of element-wise spacetree traversals is a classic non-overlapping domain decomposition. Each cell in the fine grid is assigned to a unique rank, while vertices along the domain boundary are replicated on each adjacent rank. Two options exist how to handle coarser levels [55]: We can hold a refined spacetree cell on any rank that also holds one of its children. Such a bottom up construction of ownership implies that refined spacetree nodes are replicated on multiple ranks—we are not non-overlapping in a multiscale sense—and that vertices

can be replicated on more than  $2^d$  ranks. Notably, it implies that each rank holds the spacetime’s root. Alternatively, we can assign a refined spacetime cell uniquely to one of the set of ranks that hold one its children (Fig. 5). Such a bottom-up construction yields a non-overlapping domain decomposition on each and every level. It implies that each cell has a unique owner, that vertices are adjacent to at most  $2^d$  ranks, that there is a logical tree topology induced on the MPI ranks, and that most ranks holds only a fragment of the overall spacetime. In our implementation, we follow the latter approach though all data flow insights holds for both approaches.

We assume that all replicated data, i.e. all values and stencils stored within the vertices, are consistent after the initial grid construction. All element-wise stencil evaluations can be done without communication on all ranks holding a cell. This yields a rank-local partial residual. If cells are held redundantly, also the partial results are determined redundantly. As soon as the local residual on a domain boundary vertex is accumulated, we send out this residual to all other ranks that hold a copy of this vertex and continue the rank-local spacetime traversal. A traversal realization that sticks to the single-touch policy for the unknowns and hides data exchange behind computation postpones the update of a vertex’s unknown. i.e. no update of unknowns is conducted right away. Instead, we retain the residual in-between two grid traversals and add a prelude to the vertex’s load process of the subsequent traversal. Data is sent out when a vertex has been processed for the last time, but it is not merged into data structures prior to the subsequent grid traversal. The prelude receives all residual contributions from all other adjacent ranks, adds them to the local residual and performs the unknown update. If we had redundant cells, the accumulation of the residual has to anticipate that some residual fragments might be determined multiple times.

The postponing of unknown updates decreases the speed of the smoother by one grid sweep in total. Amortized over all sweeps, our parallelization does not alter the convergence speed. In return, the data exchange can be realized in a non-blocking manner in the background. However, we experience a slight reduction of the speed along grid resolution changes. Our FAS-based handling of coarser grid regions requires the injected fine-grid solution. If the smoother’s fine grid updates are postponed to the subsequent iteration, no valid injected data from the current iteration is available there yet. In the parallel code, updates are injected into coarser levels one sweep later than in the serial case. This has an impact on smoothers working on adaptive grids. At hands of the domain decomposition description of such smoothers, we see that the fine-to-coarse domain coupling is delayed while the coarse-to-fine coupling through interpolation along the hanging vertices remains tight.

While a relaxed inter-level coupling is acceptable, we face a more severe data consistency challenge throughout the reduction of the multiplicative algorithm. The hierarchical residuals—partially computed along the domain boundaries—are restricted per rank. The restricted values then are exchanged to determine the right-hand side for the coarse grid correction. This postponed data flow scheme mirrors the exchange of residuals. Our serial/shared memory algorithms propose to fuse the coarse grid smoothing with the restriction. This relies on the facts that (i) the right-hand side is correctly restricted when a vertex is used for the last time throughout a traversal, (ii) the matvec accumulation of the correction is independent of the right-hand side, and (iii) the fine grid computation of  $\hat{r}$  has no influence on the injected coarse grid representation  $u_{\ell-1} = Iu_\ell$ . Obviously, constraint (i) and (ii) are shifted to the begin of the subsequent grid sweep in our scheme. Through this, constraint (iii) is harmed.

We thus run  $\mu_{pre}$  pre-smoothing steps per level, and then add an additional grid traversal to complete the smoothing, inject the solution to the next coarser grid and restrict the right-hand side locally. The partially restricted right-hand sides are sent out at the end of the grid sweep

and thus are available on remote ranks once the first smoothing step on the coarser level starts. This break-up of smoothing and restriction into two separate grid traversals reduces the solver efficiency—additional  $\ell_{max} - \ell_{min}$  grid sweeps are required per V-cycle—but it allows us to keep the right-hand sides consistent. No data consistency problems arise during the steps down within the V-cycle as we realize our multigrid solver within depth-first tree traversals.

**Observation 11** *We have to invest one additional grid sweep per multigrid restriction in the multiplicative case. Otherwise, the data consistency can not be preserved with data exchange in the background of the computation.*

Our algorithm exchanges two doubles per refined vertex ( $r$  and  $b$ ) and only the residual for fine-grid vertices. For the dynamic adaptivity criterion, additional quantities are exchanged. While the exchanged attribute cardinality is low, it is important to recognize that the two residuals on boundary vertices now have to be stored persistently. Without MPI, we are able to discard them after each traversal. This increases the memory footprint along domain boundaries.

The Galerkin coarse grid stencils are computed additively over cells. Consequently, we may send out the partial stencils in the synchronization traversal and receive and accumulate them in the preamble of the follow-up smoothing sweep. BoxMG determines  $P$  and  $R$  through local patch computations. While we use a non-overlapping multiscale domain decomposition, we weaken this concept and replicate those cells required to compute all patch operations on one rank. Consequently, the *descend* event requires no special attention. Along the boundary, all rank-local *descends* yield solely partial inter-grid transfer operators. As BoxMG computes entries along a patch boundary redundantly—this statement also holds for injection and trivial aggregation—all entries affecting local vertices are always available.

Additive multigrid is sketched in [40] and can be realized following the present data flow ideas as long as no FAS is employed. If we use FAS, Observation 11 immediately implies that the scheme runs into inconsistent data. A solution to this approach is the pipelining approach from [42] that also fixes the weakened domain coupling of meshes of different resolutions in the adaptive case. BPX follows these lines. It is an open question whether the pipelining concept applied to the multiplicative setup yields a realization that is superior to the present approach with an additional grid sweep per restriction step.

We conclude our distributed memory discussion with the observation that our code family keeps redundantly held vertex data consistent—if required by additional spacetime sweeps. As a consequence, stencil compression can be applied in parallel on boundary vertices, too, where it yields the same compression factors for redundantly held grid entities. It is a straightforward decision thus to exchange the compressed byte streams instead of the real stencils.

## 7 Results

Our benchmarks study (1) with the parameter sets from Table 3. To realize dynamic adaptivity, we evaluate the mean value of the  $3^d - 1$  surrounding vertices per non-hanging vertex and compute the absolute value of the difference of this mean value to the actual vertex value. The feature-based criterion assumes that refinement pays off where the problem changes rapidly, i.e. where this difference is significant. A region around a vertex is a refinement candidate if the vertex is unrefined and if the residual in the particular vertex falls below  $10^{-2}$ . Per grid sweep, we refine the 10 percent of the candidates with the biggest absolute mean value differences as long as the

Table 3: Overview of the benchmark parameter sets for (1).

Identifier	sin	jump	checkerboard
$f$	$2\pi^2\Pi_i\sin(\pi x_i)$	1	1
$u _{\partial\Omega}$	0	0	0
$v$	0	0	0
$\epsilon$	1	$\begin{cases} 1 & \text{if } x_1 < 0.5 \\ 0.1 & \text{otherwise} \end{cases}$	$\epsilon_i = \begin{cases} 1 & \text{if } x_i < 0.5, \\ 0.1 & \text{otherwise} \end{cases}$

---

Identifier	circle
$f$	0
$u _{\partial\Omega}$	$\begin{cases} 1 - 4(x_2 - 0.5)^2 & \text{if } x_1 = 0 \vee x_1 = 1 \\ 0 & \text{otherwise} \end{cases}$
$v$	$\begin{pmatrix} \sin(\pi x_2 - 0.5)\cos(\pi x_1 - 0.5) \\ -\cos(\pi x_2 - 0.5)\sin(\pi x_1 - 0.5) \\ 0 \end{pmatrix}$
$\epsilon$	$\begin{cases} \{10^{-1}, 10^{-2}, 10^{-3}, 10^{-4}\} & \text{if } x_3 \leq 0.5 \text{ or } d = 2 \\ 1 & \text{otherwise} \end{cases}$

minimal mesh width permits. To avoid a global sorting step per iteration, our code uses binning with ten bins, with each bin representing a certain range of the refinement criterion’s differences. This range is adapted after each traversal as we keep statistics per bin on how many vertices fit into it. All vertices fitting into the bin representing the mean value difference are refined—the 10 percent goal is approximated.

All experiments were conducted on a cluster with Intel E5-2650V4 (Broadwell) nodes with 24 cores per node. They run at 2.4 GHz. Furthermore, we reran the multicore experiments on an Intel Knights Landing chip (Xeon Phi 7250) at 1.4 GHz. For the shared memory parallelization, we rely on Intel’s Threading Building Blocks (TBB). For the distributed memory parallelization, we use Intel MPI. Intel’s C++ compiler 2017 version 2 translates all codes. The realization is based on the spacetime PDE framework Peano [57]. As we stick to a low order discretization on dynamically adaptive meshes and do not exploit any mesh regularity, we only exploit the compiler’s vectorization of the BoxMG matrix-vector products. Further vectorization along the lines of [42] for multi-parameter runs or [24] for grids with some (patch) regularity is beyond scope.

## 7.1 Diffusion with constant coefficients

An analytical solution is known for the `sin` benchmark. Geometric rediscretization yields the Galerkin coarse-grid operator if  $d$ -linear prolongation and restriction are chosen that BoxMG yields. The setup thus acts as validation scenario.

All required records per vertex are enlisted in Table 2. For the pure geometric solver, we only hold three or four, respectively, doubles per grid vertex. Exhaustive search over potential relaxation parameters for the additive solver results in  $\omega \approx 0.8$ , yielding reasonable convergence rates though no relaxation or slight overrelaxation is even faster (Table 4). As soon as we switch to a dynamically

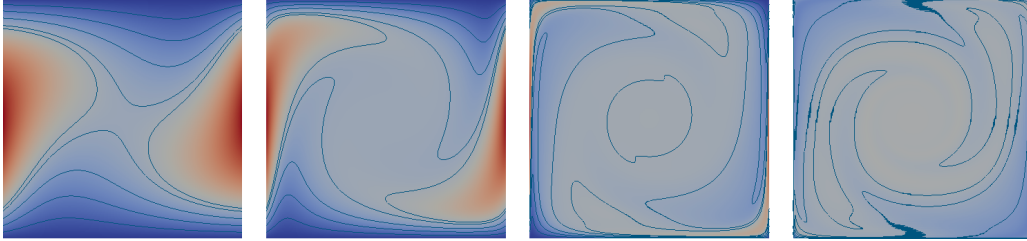


Figure 6: Solution of the `circle` problem (Table 3) for  $d = 2, \epsilon \in \{10^{-1}, 10^{-2}, 10^{-4}, 10^{-8}\}$  (left to right) with isolines at  $u \in \{0.1, 0.2, 0.3, 0.4, 0.44\}$ .

Table 4: Number of grid sweeps for additive multigrid that are required to reduce the residual for the `sin` benchmark (Table 3) by a factor of  $10^{-8}$ . The sections show  $d = 2$  (top) and  $d = 3$  (bottom) with  $\omega = 0.8$ . All experiments are computed on regular Cartesian grids spanned by the spacetree, i.e. we build up the whole grid and then start the solve. The tuples denote cycle counts with exponential damping (left) and undamped coarse grid relaxation (right). Jac denotes a Jacobi smoother, BJ is a block Jacobi with the number of Gauß-Seidel sweeps per block in brackets. The /e postfix implies that we use an exact coarse grid solve.

h	Jac	BJ(1)	BJ(2)	BJ(4)	BJ(8)	Jac/e	BJ(1)/e	BJ(2)/e	BJ(4)/e	BJ(8)/e
$3^{-2}$	34/26	19/19	16/16	13/13	12/12	34/26	16/16	13/13	12/12	12/12
$3^{-3}$	48/41	24/22	20/18	17/18	17/18	48/41	22/21	19/18	17/18	17/18
$3^{-4}$	63/44	29/24	24/21	22/21	22/21	63/44	27/23	24/21	22/21	22/21
$3^{-5}$	82/47	34/24	30/23	28/23	28/23	82/47	33/24	30/23	28/23	28/23
$3^{-6}$	98/45	41/25	37/26	35/26	35/26	98/45	40/25	37/25	35/26	35/26
$3^{-2}$	21/19	19/19	17/17	17/17	17/17	21/19	17/17	17/17	17/17	17/17
$3^{-3}$	42/39	26/25	23/22	22/22	22/22	42/39	25/24	23/22	22/22	22/22
$3^{-4}$	51/39	32/27	29/25	29/25	28/25	51/39	31/27	29/25	29/25	28/25

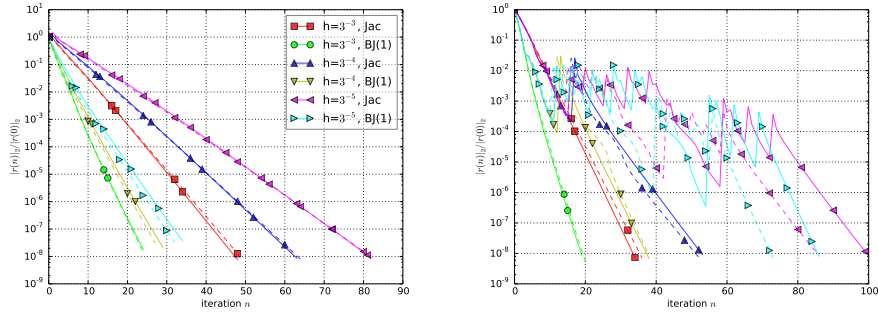


Figure 7: Convergence behaviour of additive multigrid with exponential damping for the `sin` benchmark on regular grids (left) and dynamically adaptive grids (right) with  $\omega = 0.8$  and  $d = 2$ . Dynamical implies that we start F-cycle like with a coarse grid and leave it to the refinement criterion to yield the final mesh. Solid lines show results for Algorithm 2 compared to a synchronized variant from [42] (dotted lines).

adaptive solver, we find that  $\omega \geq 1.0$  becomes unstable. Thus, we stick to  $\omega = 0.8$  from hereon. Better convergence rates might be obtained for alternating relaxation parameters, where we use a different parameter for each sweep. We refer to [33] for some symbol analysis or [42] for a Helmholtz example. If we damp  $\omega$  exponentially—use  $\omega$  on the finest grid,  $\omega^2$  on the first coarse grid, and so forth—we harm the speed. However, we obtain a stable scheme, while otherwise the additive solver tends to overshoot [8, 42]. The speed gap between exponential  $\omega$  damping and smoothing with uniform relaxation factor narrows if we use a block smoother, but it does not close completely. Block smoothers can double the convergence speed, but more than four Gauß-Seidel block sweeps rarely pay off. An exact coarse grid solve does not pay off for the additive solvers.

In Algorithm 2, fine-grid updates are immediately injected to the coarser grids. In turn, coarse-grid computations might work with outdated coarse solutions, which change during the element-wise assembly. Our experiments show that this inconsistency does not make a difference for regular grids (Fig. 7). It, however, slightly deteriorates the convergence for adaptive grids. Here, we start from  $h = 3^{-1}$  and make the adaptivity criterion add further vertices. The effect is studied and a single-touch solution is proposed in [42], and we conclude for our experiments that their multilevel synchronization with pipelining should be used.

All statements on additive solvers also hold for BPX, besides the fact that an exact coarse grid solve here has no major positive impact (Fig. 8). In general, BPX from Algorithm 3 outperforms the additive solver. Block smoothing pays off. The impact of block smoothing on multiplicative multigrid is even more significant. For the latter, exact coarse-grid solves are advantageous and we need 10–15 iterations in total.

**Observation 12** *Our experiments validate at hands of the `sin` benchmark that all three algorithm variants yield multigrid behaviour.*

Next we compare the residual reduction to unknown reads from memory. The latter scale with `touchVertexFirstTime` counts. Block operations and accumulations all are expected to happen in the cache due to the vertical integration of the algorithm’s phases within one tree sweep [58]. We

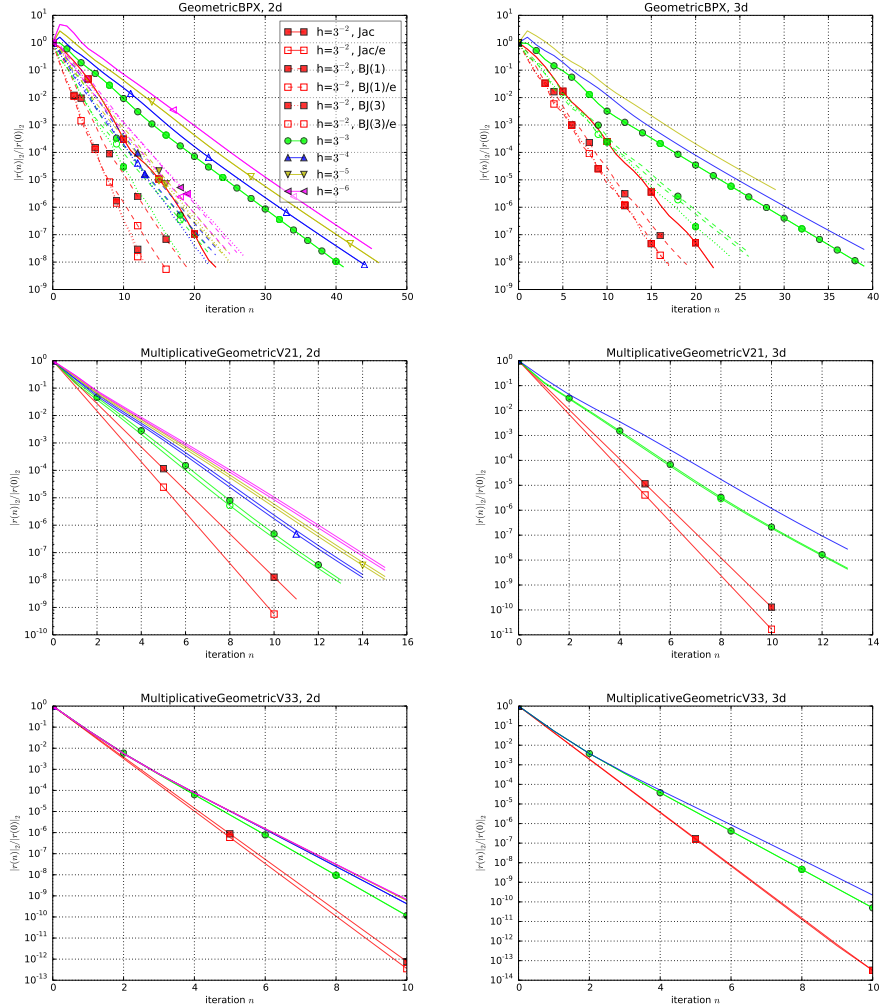


Figure 8: Convergence of various solvers for the `sin` benchmark on regular grids with  $\omega = 0.8$ . Solid lines with filled symbols use a Jacobi smoother, dashed lines use block Jacobi with one Gauß-Seidel sweep, and dotted lines apply three sweeps. Empty symbols furthermore are for solving the coarse-grid problem exactly while solid symbols are for applying only  $\mu_{pre} + \mu_{post}$  sweeps on the coarsest grid.

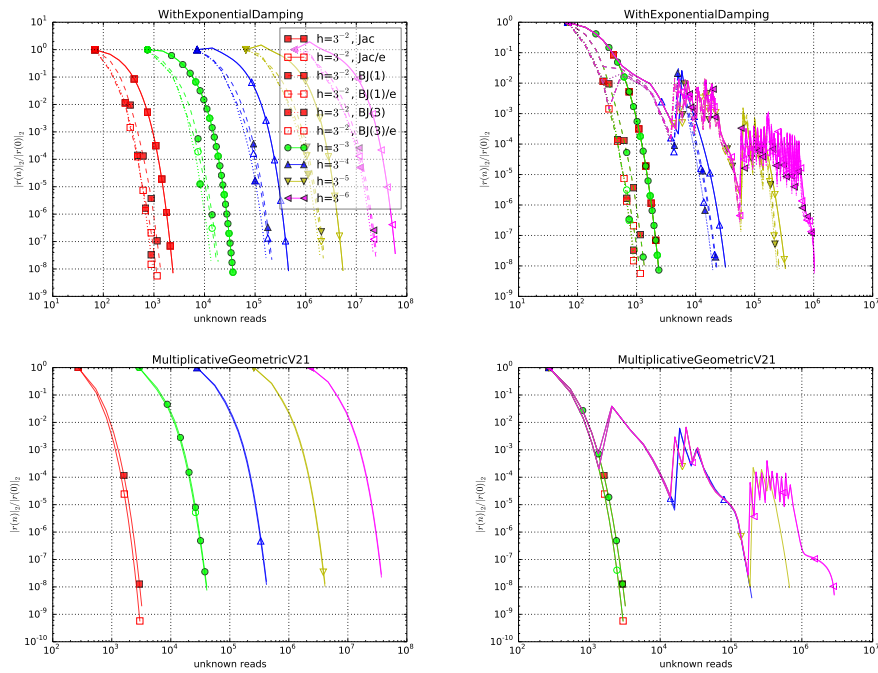


Figure 9: Cost in terms of unknown reads for the  $\sin$  benchmark with  $\omega = 0.8$  and  $d = 2$ . Regular grids (left column) are compared to grids that unfold dynamically through the adaptivity criterion (right). The additive solver (top) is slower by a factor of one up to two compared to BPX (not shown) which is in the same order of cost as the multiplicative variant (bottom).

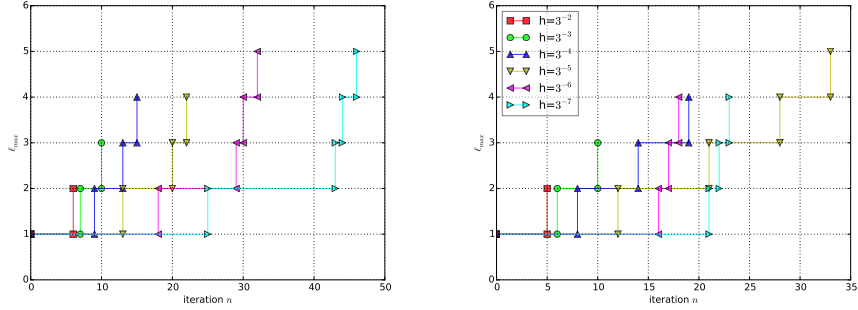


Figure 10: Development of  $\ell_{max}$  over the number of iterations if the algorithm is allowed to increase the coarsest level whenever the residual for the  $2d$  version of the `jump` benchmark starts to grow. Data for geometric BPX with the `BlockJacobi(4)` smoother (left) and multiplicative V11 with Jacobi smoothers (right).

validate this theoretic statement experimentally in Sect. 7.6. Multiplicative solvers are superior to the other solver variants. However, the vast difference in iteration counts does not translate directly into speed/data reads—the difference in actual runtime is smaller (Fig. 9). All variants yield cost in the same order of magnitude.

**Observation 13** *For the smooth `sin` setup, multiplicative multigrid is not significantly superior to additive variants in terms of memory access cost.*

We observe an opposite effect regarding cost vs. iteration count in Fig. 9: The dynamic adaptivity unfolds the grid in a full multigrid (FMG) way for BPX and the additive solver and naturally yields FMG character lacking higher-order operators. This decreases the time-to-solution yet increases the iteration count.

**Observation 14** *For a very smooth setup such as in the `sin` benchmark, a dynamic refinement criterion unfolding the grid from a coarse start solution yields almost  $F$ -cycle-like convergence even in the absence of higher order interpolation.*

## 7.2 Jumping and anisotropic material parameters $\epsilon$

We continue with the `jump` setup, where the material parameter changes in the middle of the domain. The change/jump is not aligned with the grid. For the geometric multigrid variants, any coarse-grid update’s  $d$ -linear interpolation  $Pd_{\ell-1}$  that overlaps the parameter jump does not anticipate the lack of smoothness in the solution and, thus, introduces a localized fine-grid error around the material parameter transition. If we project update from left and right of the jump, the update’s linear interpolation lacks the discontinuity in the derivative, it pollutes the solve around the  $\epsilon$  jump. For reasonable big  $\omega$ , the solvers start to oscillate locally.

The problem can be tackled by stronger smoothers or higher  $\mu$  counts applied to the finest grids, or we can use smaller  $\omega$ . Both approaches harm multigrid performance. They furthermore suffer from the fact that it is often not clear which  $\ell_{max}$  still yields a robust solver for a particular setup.

Table 5: Iteration counts for the additive multigrid, additive multigrid with exact coarse-grid solve, and BPX (left to right) with  $\omega = 0.8$  solving the `jump` benchmark for  $d = 2$ .  $\perp$  is used to denote that a solver was not able to reduce the residual by a factor of  $10^8$  within 300 iterations.

h	Jac	BJ(1)	BJ(2)	BJ(4)	BJ(8)	Jac/e	BJ(1)/e	BJ(2)/e	BJ(4)/e	BJ(8)/e	Jac	BJ(1)	BJ(2)	BJ(4)	BJ(8)
$3^{-2}$	62	41	36	35	34	$\perp$	41	36	35	34	62	41	36	35	34
$3^{-3}$	90	58	52	49	49	$\perp$	57	52	49	49	76	52	47	44	44
$3^{-4}$	131	81	72	68	67	$\perp$	79	71	68	67	96	67	60	57	56
$3^{-5}$	179	106	93	88	87	$\perp$	103	93	88	87	$\perp$	81	72	68	67
$3^{-6}$	201	120	108	103	102	$\perp$	119	108	103	102	$\perp$	85	77	73	72
$3^{-7}$	$\perp$	123	112	107	106	$\perp$	123	112	107	106	$\perp$	80	73	70	69

Table 6: Iteration counts for the `jump` and  $d = 2$  with multiplicative V21-cycle.  $\perp$  denotes that a solver is not able to reduce  $|r|_2$  by a factor of  $10^8$  within 300 iterations.

h	Jac	BJ(1)	BJ(2)	BJ(4)	BJ(8)	Jac/e	BJ(1)/e	BJ(2)/e	BJ(4)/e	BJ(8)/e
$3^{-2}$	21	14	12	12	12	$\perp$	14	12	12	12
$3^{-3}$	27	20	18	18	18	$\perp$	20	18	18	18
$3^{-4}$	35	27	25	24	24	$\perp$	27	25	24	24
$3^{-5}$	42	34	32	31	30	$\perp$	34	32	31	30
$3^{-6}$	42	35	33	32	32	$\perp$	35	33	32	32
$3^{-7}$	$\perp$	33	31	30	30	$\perp$	33	31	30	30

Our code family identifies non-diagonal dominant operators, stagnation or amplifying oscillations, increases the coarsest mesh level  $\ell_{max}$  autonomously and thus avoids some instabilities (Fig. 10). Yet, we are not able to solve any setup from the `jump` benchmark with less than 300 iterations with Jacobi once  $h < 3^{-2}$ . For  $h = 3^{-2}$ , the additive multigrid with a 4-sweep block smoother requires already 133 iterations—it deteriorates. In general, the  $\ell_{max}$  modifications remove more coarse grid resolutions from the additive and BPX schemes than for the multiplicative multigrid, while the increase of  $\ell_{max}$  does not kick in for any Galerkin solver variant:

**Observation 15** *An adaptive coarse grid choice mitigates the effect of the absence of Galerkin coarse grid operators w.r.t. stability and, at the same time, identifies the coarsest resolution level where geometric multigrid remains robust. With respect to the performance, it remains a workaround in the absence of proper unstructured coarse grids or algebraic/direct coarse grid solves.*

Experiments reveal that the problem can be solved in around 107 iterations ( $h = 3^{-7}$ ) if we use Galerkin coarse-grid operators and block smoothers. BPX converges in 35 ( $h = 3^{-2}$ ) to 70 ( $h = 3^{-7}$ ) iterations (Table 5). We recognize that a grid spacing reduction from  $3^{-6}$  to  $3^{-7}$  reduces the total iteration count here: in regions of interest the grid is refined aggressively, but if the maximum level is too constrained, these regions spread out and increase the vertex count unnecessarily. This anomaly carries over to multiplicative multigrid (Table 6), which now clearly outperforms the other two solvers. An exact coarse-grid solve now does not pay off anymore. Though the solver remains stable with  $\ell_{max} = 1$ , the coarsest level can not contribute with any useful correction as it is too coarse. As an improvement, one could choose a larger  $\ell_{max}$  right from the start and solve exactly there.

Dynamic adaptivity again pays off (Table 7) and reduces the number of unknown reads by an order of magnitude: the grid quickly refines around the material transition and, thus, injects the critical behaviour into the coarse-grid corrections. At the same time it acts as FMG facilitator.

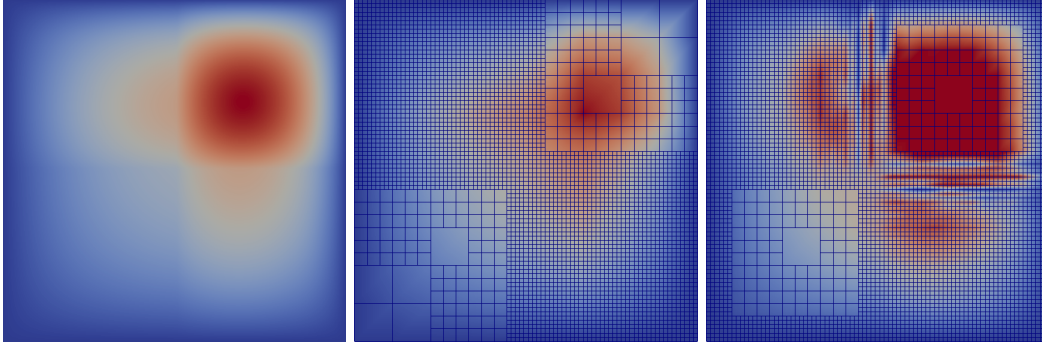


Figure 11: From left to right: Solution of the **checkerboard** setup for  $d = 2$ . Typical adaptive grid. Instability pattern arising from additive geometric multigrid with rediscretization after 28 iterations.

Table 7: Cost (number of unknown reads) of experiments of Table 6 with regular grid (top) and the dynamically adaptive grid (bottom).

h	Jac	BJ(1)	BJ(2)	BJ(4)	BJ(8)
$3^{-2}$	5.90e+03	4.02e+03	3.48e+03	3.48e+03	3.48e+03
$3^{-3}$	8.14e+04	6.11e+04	5.53e+04	5.53e+04	5.53e+04
$3^{-4}$	1.00e+06	7.79e+05	7.24e+05	6.96e+05	6.96e+05
$3^{-5}$	1.10e+07	8.95e+06	8.44e+06	8.18e+06	7.93e+06
$3^{-6}$	9.96e+07	8.34e+07	7.88e+07	7.65e+07	7.65e+07
$3^{-2}$	⊥	4.02e+03	3.48e+03	3.48e+03	3.48e+03
$3^{-3}$	⊥	4.02e+03	3.48e+03	3.48e+03	3.48e+03
$3^{-4}$	⊥	3.58e+04	3.37e+04	3.17e+04	3.17e+04
$3^{-5}$	⊥	6.35e+06	6.35e+06	6.31e+06	6.31e+06
$3^{-6}$	⊥	⊥	5.12e+06	5.10e+06	5.10e+06

Table 8: Number of iterations to solve the **checkerboard** benchmark with additive multigrid (left,middle) and BPX (right) for  $d = 2$ . All inter-grid transfer operators are bilinear, coarse-grid operators realize the Galerkin idea.

h	Jac	BJ(1)	BJ(2)	BJ(4)	BJ(8)	Jac/e	BJ(1)/e	BJ(2)/e	BJ(4)/e	BJ(8)/e	Jac	BJ(1)	BJ(2)	BJ(4)	BJ(8)
$3^{-2}$	120	67	57	52	51	120	68	57	52	51	115	67	57	52	51
$3^{-3}$	270	117	91	80	78	270	118	91	79	78	⊥	116	91	79	78
$3^{-4}$	⊥	140	112	100	98	⊥	137	111	100	98	⊥	136	107	94	92
$3^{-5}$	⊥	163	132	118	116	⊥	158	129	118	116	⊥	146	116	102	100
$3^{-6}$	⊥	167	140	130	129	⊥	166	140	130	129	⊥	137	113	102	101
$3^{-7}$	⊥	156	135	127	125	⊥	⊥	⊥	⊥	⊥	⊥	119	101	92	91

Table 9: Experiments from Table 8 with multiplicative V21 cycle.

h	Jac	BJ(1)	BJ(2)	BJ(4)	BJ(8)	Jac/e	BJ(1)/e	BJ(2)/e	BJ(4)/e	BJ(8)/e
3 <sup>-2</sup>	44	23	18	16	16	44	23	18	16	16
3 <sup>-3</sup>	⊥	40	32	29	29	⊥	40	32	29	29
3 <sup>-4</sup>	⊥	49	42	39	39	⊥	49	42	39	39
3 <sup>-5</sup>	⊥	58	52	50	49	⊥	58	52	50	49
3 <sup>-6</sup>	⊥	56	51	50	49	⊥	56	51	50	49
3 <sup>-7</sup>	⊥	50	47	46	45	⊥	50	47	46	45

Table 10: Cost for the experiments of Table 9 with regular (left) or dynamically adaptive grid (right).

h	Jac	BJ(1)	BJ(2)	BJ(4)	BJ(8)	Jac	BJ(1)	BJ(2)	BJ(4)	BJ(8)
3 <sup>-2</sup>	1.21e+04	6.43e+03	5.09e+03	4.56e+03	4.56e+03	1.21e+04	6.43e+03	5.09e+03	4.56e+03	4.56e+03
3 <sup>-3</sup>	⊥	1.19e+05	9.60e+04	8.72e+04	8.72e+04	1.21e+04	6.43e+03	5.09e+03	4.56e+03	4.56e+03
3 <sup>-4</sup>	⊥	1.39e+06	1.20e+06	1.11e+06	1.11e+06	⊥	7.63e+04	5.80e+04	5.05e+04	5.05e+04
3 <sup>-5</sup>	⊥	1.51e+07	1.36e+07	1.30e+07	1.28e+07	⊥	1.13e+06	9.98e+05	9.79e+05	9.63e+05
3 <sup>-6</sup>	⊥	1.32e+08	1.20e+08	1.18e+08	1.16e+08	⊥	4.63e+06	4.59e+06	4.55e+06	4.55e+06

Empty entries in Table 7 result from the fact that we always stop after 300 iterations; an iteration count that is quickly met if grid “setup” iterations are counted as part of an FMG cycle.

Our follow-up experiments with the `checkerboard` setup continue to have  $\epsilon$  jumps, but furthermore introduce anisotropic regions. Anisotropic behaviour poses even harder challenges to  $d$ -linear inter-grid transfer operators: All geometric solvers are ill-suited for this problem, they do not converge (Fig. 11). While the regular Galerkin solvers converge, mesh-independent convergence is lost completely (Tables 8,9). Again, an exact coarse-grid solve in the multiplicative setting is not required: no matter how exact the coarsest problem is solved, the prolongation of the correction always yields wrong fine-grid modes for varying  $\epsilon$  or anisotropic  $\epsilon_i \neq \epsilon_j$ .

The dynamic adaptivity criterion continues to make a dynamic approach outperform its regular-grid counterpart in terms of cost (Table 10), while the actual number of grid sweeps is higher by a factor of four. Yet, the sweeps are cheap as long as the grid has not unfolded substantially. Due to the irregularity of `checkerboard`, the feature-based adaptivity refines anisotropic regions, regions around  $\epsilon$  changes and along the boundary (Fig. 11).

**Observation 16** *Our global, uniform choice of a smoothed grid level where fine grid regions coarser than the current smoothing level are updated per cycle, too, plus the dynamic refinement criterion being active in each cycle imply that rough solution regions are subject to immediate refinement. At the same time, smooth regions resolved by a rather coarse grid are subject to more smoothing steps.*

### 7.3 BoxMG

The recirculating flow problem `circle` (Table 3) with inflow boundary conditions from the left and right side (Fig. 4) introduces non-zero convection which destroys the symmetry of  $A$ . The smaller the (symmetric) diffusion weight  $\epsilon$  of the operator relative to the convection the more challenging the setup becomes for multigrid solvers. They struggle with convection-dominated systems (Fig. 6). In our setup, the convection coefficients furthermore vary in space and there is a singularity in the middle of the domain. Finally, the closed characteristics prevent any solver error from being “pushed out” of the domain by relaxation. Geometric multigrid and Galerkin multigrid with  $d$ -

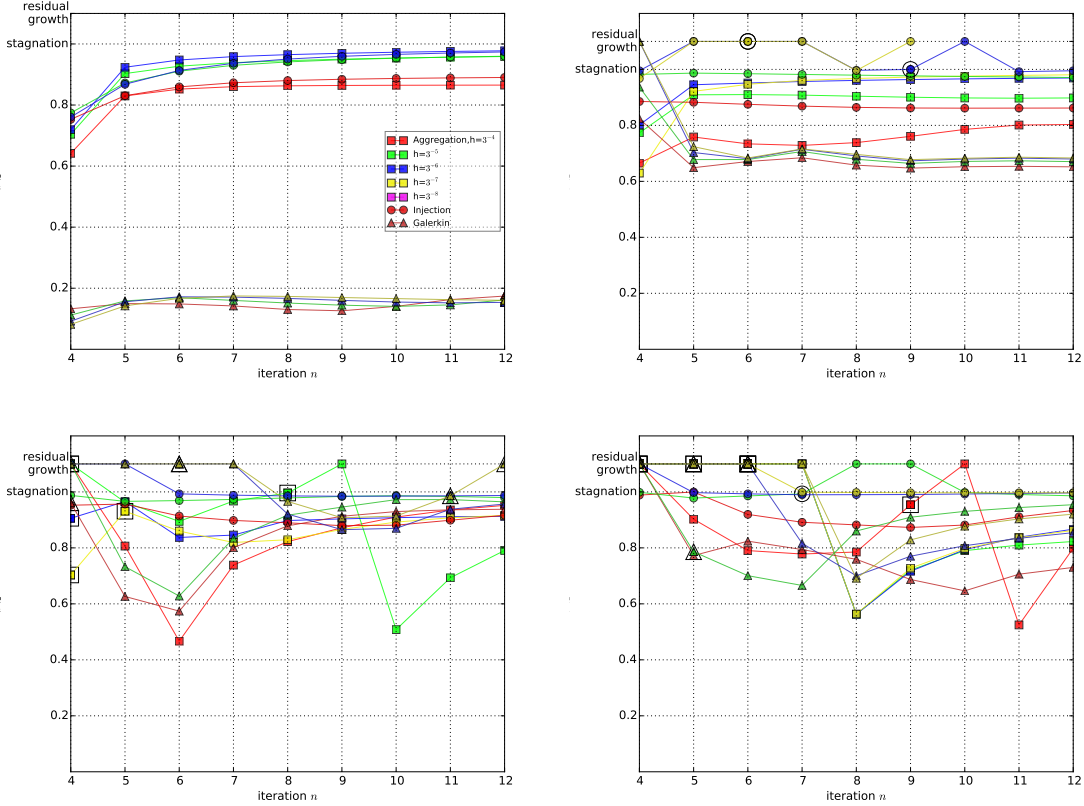


Figure 12: Convergence speed  $\rho = |res(n)|_2/|res(n-1)|_2$  as ratio between current residual to residual of previous iteration. The experiments pass  $\epsilon = \{10^{-1}, 10^{-2}, 10^{-4}, 10^{-8}\}$  (left to right, top-down) into a V21 multigrid with a block Jacobi smoother running four iterations per patch. Large empty symbols indicate that the solver increases  $\ell_{max}$  in that iteration.

linear inter-grid transfer operators solve this problem if we use dynamic coarse-grid adaptation and proper upwinding. However,  $\ell_{max}$  increases fast and, hence, the solvers transition quickly into pure (block) Jacobi.

Once we supplement the Galerkin coarse grid operator computation with BoxMG, we obtain a more robust solver. To show this, we track the convergence speed  $\rho(n)$  as ratio of the residual norm in an iteration  $n$  relative to the residual norm in the iteration  $n-1$  (Fig. 12). Furthermore, we compare plain BoxMG with a Petrov-Galerkin scheme where  $R = I$  (injection) or  $R$  is an aggregation operator. We observe the convergence speed deteriorates with decreasing  $\epsilon$ , i.e. with an increasing impact of the convection, for all solvers. We start loosing multigrid behaviour. Convergence speed depends on the mesh size, and measurements for one type of solver (same symbol) fan out. For  $\epsilon = 10^{-1}$  the automatic coarse grid increase is not triggered. The solvers work with  $\ell_{max} = 1$  all the time. The smaller  $\epsilon$  the more often  $\ell$  is increased. Injection yields consistently the worst

Table 11: Overview of the solver variants and their performance for the different problem setups. A checkmark indicates that the problem can be solved by the respective solver with multigrid performance, a checkmark in brackets indicates that the solver converges, but mesh-independent (multigrid) performance is lost. A cross denotes that the solver diverges for the problem. For **circle**, the behaviour depends strongly on the weight of the convection term relative to the diffusion.

	<b>sin</b>	<b>jump</b>	<b>checkerboard</b>	<b>circle</b>
Geo. Add.	✓	(✓)	×	×
Geo. BPX	✓	(✓)	×	×
Geo. Mult.	✓	(✓)	×	×
Galerkin. Add.	✓	✓	(✓)	×
Galerkin. BPX	✓	✓	(✓)	×
Galerkin. Mult.	✓	✓	(✓)	×
BoxMG Add.	✓	✓	✓	✓ to (✓)
BoxMG BPX	✓	✓	✓	✓ to (✓)
BoxMG Mult.	✓	✓	✓	✓ to (✓)

convergence speed and is thus not studied further. We can not identify a significant reduction of the number of  $\ell_{max}$  increases if we switch from pure BoxMG to the symmetric aggregation-based restriction. While literature would expect us to obtain more stable coarse grid operators (cmp. the discussion in [61] and references therein), we do not observe this effect here—probably due to a lack of a higher order symmetric operator. However, we do observe that aggregation yields slightly better convergence rates than a pure Galerkin approach with  $P = R^T$  if the grid is sufficiently fine and  $\epsilon$  is small enough.

A study of the exact behaviour of the various multigrid compositions (Table 11) is beyond scope here though we state that the BoxMG solvers are reasonably robust to tackle non-trivial problems. Yet, the experiments also illustrate that stronger smoothers such as ILU, Kaczmarz or alternating line Gauss-Seidel are highly desirable for dominating convection. Keeping this in mind, our ideas can act as a reasonable code building block for robust solvers on spacetimes that work strictly element-wise and matrix-free. All solvers implement a single-touch policy, i.e., one tree traversal realizes one multigrid cycle (additive and BPX) or smoothing step (multiplicative). In practice, this means that a multiplicative cycle is by a factor of  $(\mu_{pre} + \mu_{post})$  times slower than an additive cycle. Both the problem character and the multigrid’s role—is it used as solver or as preconditioner—determine which approach is superior in terms of time to solution. A generic “better than” statement is impossible to make.

## 7.4 Memory consumption

To quantify the memory demands, we study dynamically adaptive grids with a multiplicative V11-BoxMG solver. Our measurements compare an uncompressed version with  $\epsilon_{mf} \in \{10^{-2}, 10^{-4}, 10^{-8}\}$ . The memory savings are enormous for the **sin** benchmark where all operators are well-known to reduce to their rediscretization or  $d$ -linear counterpart. With decreasing  $h$ , the code becomes matrix-free.

For the **jump** and **circle** setups, we preserve significant memory savings, though they are by a factor of two to four smaller than for the **sin** setup. We may choose rather small  $\epsilon_{mf} = 10^{-8}$  and nevertheless obtain both high compression rates and preserve the solvers’ semantics. If the compression is too aggressive, the adaptivity criterion yields slightly different adaptivity patterns,

Table 12: Multiplicative BoxMG with dynamic adaptivity criterion for  $d = 2$  and **sin** (top), **jump** and **circle** (bottom). We present one tuple per run. The left entry denotes how many vertex updates are required to reduce the residual to  $10^{-8}$ , while the right entry gives the memory footprint with compressed algebraic operators relative to the uncompressed run.

h	0	1e-2	1e-4	1e-8
$3^{-3}$	2.24e+03 / 1.0	2.24e+03 / 1.33e-02	2.24e+03 / 1.99e-02	2.24e+03 / 3.31e-02
$3^{-4}$	1.36e+05 / 1.0	1.27e+05 / 5.68e-03	2.06e+05 / 8.35e-03	1.36e+05 / 1.38e-02
$3^{-5}$	1.37e+05 / 1.0	2.97e+05 / 4.28e-03	4.57e+05 / 5.12e-03	1.37e+05 / 1.39e-02
$3^{-6}$	2.09e+06 / 1.0	2.92e+06 / 2.83e-03	2.09e+06 / 4.39e-03	2.09e+06 / 7.29e-03
$3^{-7}$	2.09e+06 / 1.0	4.80e+06 / 2.82e-03	2.09e+06 / 4.39e-03	2.09e+06 / 7.29e-03
$3^{-3}$	2.65e+03 / 1.0	1.02e+03 / 1.63e-02	1.84e+03 / 2.48e-02	2.65e+03 / 4.10e-02
$3^{-4}$	2.81e+04 / 1.0	4.41e+05 / 9.57e-03	2.51e+04 / 1.47e-02	2.81e+04 / 2.39e-02
$3^{-5}$	4.54e+06 / 1.0	2.72e+05 / 7.90e-03	4.54e+06 / 8.41e-03	4.54e+06 / 1.35e-02
$3^{-6}$	4.13e+06 / 1.0	2.72e+05 / 7.90e-03	4.13e+06 / 6.65e-03	4.13e+06 / 1.07e-02
$3^{-7}$	4.17e+06 / 1.0	2.72e+05 / 7.90e-03	4.18e+06 / 6.72e-03	4.17e+06 / 1.08e-02
$3^{-3}$	1.08e+04 / 1.0	5.10e+03 / 1.68e-02	7.75e+03 / 2.53e-02	2.33e+04 / 4.10e-02
$3^{-4}$	2.43e+04 / 1.0	2.41e+04 / 9.57e-03	2.43e+04 / 1.42e-02	2.43e+04 / 2.25e-02
$3^{-5}$	3.43e+05 / 1.0	2.05e+05 / 1.20e-02	3.43e+05 / 1.64e-02	3.43e+05 / 2.67e-02
$3^{-6}$	1.84e+07 / 1.0	1.78e+07 / 1.14e-02	1.60e+06 / 1.62e-02	1.84e+07 / 2.51e-02
$3^{-7}$	1.45e+07 / 1.0	1.86e+07 / 1.14e-02	1.60e+06 / 1.62e-02	1.45e+07 / 2.56e-02

Table 13: Characteristic runtimes per V22 cycle for a regular (left) and an adaptive (right) mesh on a single core for the checkerboard setup.

$h_{min}$	no compr.	compr.	no compr.	compr.
$3^{-4}$	$1.54 \cdot 10^{-2}$	$2.03 \cdot 10^{-3}$	$1.08 \cdot 10^{-2}$	$1.55 \cdot 10^{-2}$
$3^{-5}$	$6.28 \cdot 10^{-2}$	$8.92 \cdot 10^{-2}$	$2.31 \cdot 10^{-2}$	$3.49 \cdot 10^{-2}$
$3^{-6}$	$3.89 \cdot 10^{-1}$	$5.26 \cdot 10^{-1}$	$0.56 \cdot 10^{-1}$	$1.01 \cdot 10^{-1}$
$3^{-7}$	$2.74 \cdot 10^{-0}$	$3.53 \cdot 10^{-0}$	$2.42 \cdot 10^{-1}$	$1.53 \cdot 10^{-1}$

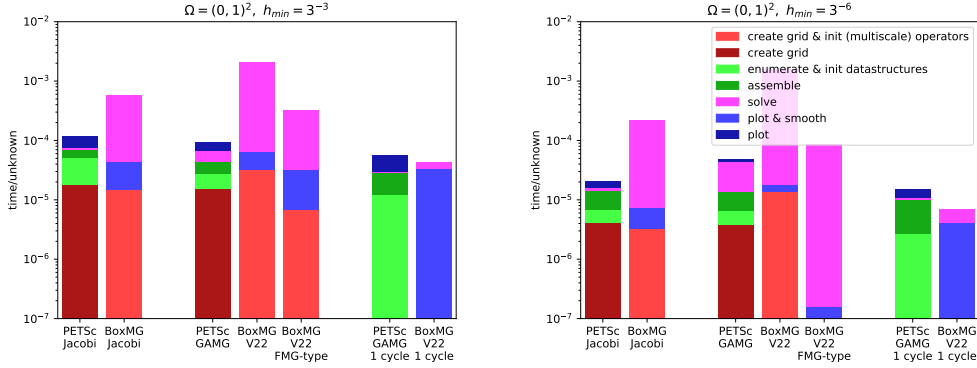


Figure 13: Comparison of the runtime of our BoxMG solver to PETSc’s GAMG solver for the checkerboard setup in  $2d$  for two different mesh sizes. We compare the cost of a Jacobi solver (single grid code), a full multigrid code, and one step of an FMG cycle.

presumably through inexact arithmetics.

Stencils plus the unknowns from Table 2 yield a memory footprint of  $3 + 3^d + 2 \cdot 5^d$  doubles plus another byte for grid management [58]. This already is a small memory footprint for dynamically adaptive grids. Compression reduces the average footprint to close to 3 doubles plus a byte per vertex without losing algebraic multigrid operators. Yet, its cost, on a single core, is not negligible (Table 13) unless the grid is extremely adaptive.

**Observation 17** *The reduction of the solver’s memory footprint to almost the pure footprint of a purely geometric approach can double the computational cost on one core.*

## 7.5 Comparisons to PETSc’s GAMG

We start our runtime studies with a brief comparison of our code’s runtime to PETSc [7] with the aggregation-based GAMG. Our naive realisation runs through the grid twice: In a first grid sweep, we enumerate the unknowns and determine the matrix sparsity pattern. In a second sweep, we assemble the matrix. A third sweep is necessary once we have solved the equation system if we want to plot the result that ties the PETSc solution to the grid. If the grid changes, a complete re-assembly with two grid sweeps becomes necessary. As we use a space-filling curve as enumeration scheme, we obtain a sparsity pattern alike Fig. 5.

We make both BoxMG and PETSc work with the same settings: PETSc’s GAMG is configured to stop once the relative residual is reduced to  $10^{-8}$ , uses a Jacobi smoother (Richardson update with Jacobi diagonal preconditioner) with  $\omega = 0.8$ , and an AMG connectivity threshold of 0.19 for its coarse grid identification is applied. This empirically chosen value yields, for the present V22-cycle, comparable coarse grids to BoxMG in terms of unknown counts.

We observe that PETSc’s explicit assembly consisting of grid construction, grid enumeration and sparsity identification plus matrix entry assembly is slightly slower than the monolithic approach of our BoxMG implementation where everything is done in one place (Fig. 13). However, we might be able to save the PETSc enumeration phase if the grid construction determined the sparsity

pattern on-the-fly. PETSc is, even though the coarse grids have to be determined algebraically and it has to maintain the coarse matrices, significantly faster than our code if we kick off from the finest grid.

The picture changes if we run a simulation where we start from a coarse grid, add (applying a refinement criterion) one level after another and thus make each solve act as prediction for the next finer solver. The picture changes if we use an FMG-type cycle. Our results show data for only two steps of such a cycle.

**Observation 18** *Our approach is able to outperform a black-box solver such as PETSc’s GAMG if and only if*

1. *the grid changes after each (or very few) solver steps,*
2. *the problem can be solved robustly with our hybrid geometric-algebraic ansatz, and*
3. *block Jacobi/Gauß-Seidel smoothers are sufficient.*

If the problem is ill-suited for our code due to a lack of robustness, our approach however may act as building block applied on the finer mesh levels while coarser problems are solved algebraically [28, 35, 43, 49]. We reiterate that such a level  $\ell_{max}$  can be determined automatically. If frequent visualisation of the solve is required, our approach also is promising as we can merge plotting and solution updates. If frequent remeshing is required and, thus, we face non-negligible assembly overhead, our approach becomes competitive. This is in line with other papers. [15], e.g., report AMG’s setup time to be equivalent to six multigrid cycles for similar algorithmic components, while in the more sophisticated setting of [51], the coarse grid and operator construction even seems to dominate the runtime.

We conclude with some memory observations made through PETSc’s `PetscMallocGetCurrentUsage` function. Our BoxMG with memory compression can reduce the memory footprint to close to 25 bytes per degree of freedom. With PETSc, the grid requires slightly more than one byte per fine grid vertex to store the linearized spacetime—the finest grid resolution level holding degrees of freedom dominates the memory footprint—plus one integer used as unknown index. These five bytes per unknown are supplemented by a total of 38 kByte PETSc administration overhead. The lion share of memory is allocated once we trigger the sparsity pattern analysis and enumeration. We end up with PETSc alone requiring between  $26.95 \cdot 3^d$  (strongly adaptive or very small grids) down to  $15.13 \cdot 3^d$  (more regular and/or large grids) bytes per degree of freedom.

## 7.6 Runtime and scalability studies

We wrap up our experiments with feasibility studies validating the parallel well-suitedness of the proposed techniques. Our shared memory study maps the dependencies from Sect. 6.1 directly onto TBB tasks. Such a naïve tactic is well-known to yield non-optimal performance as the tasks exhibit small arithmetic intensity and a significant tasking overhead. Nevertheless, we observe speedup and we are able to derive qualitative properties of the proposed scheme.

We start with  $d = 2$  runs on the Broadwell (Fig. 14) and observe that the cost of the block smoothing is negligible. All block data is cached and thus the flops for the small blocks are almost for free. Despite the fact that the grid management overhead amortizes, we observe that the cost per degree of freedom per cycle increases when we increase the number of mesh levels as additional

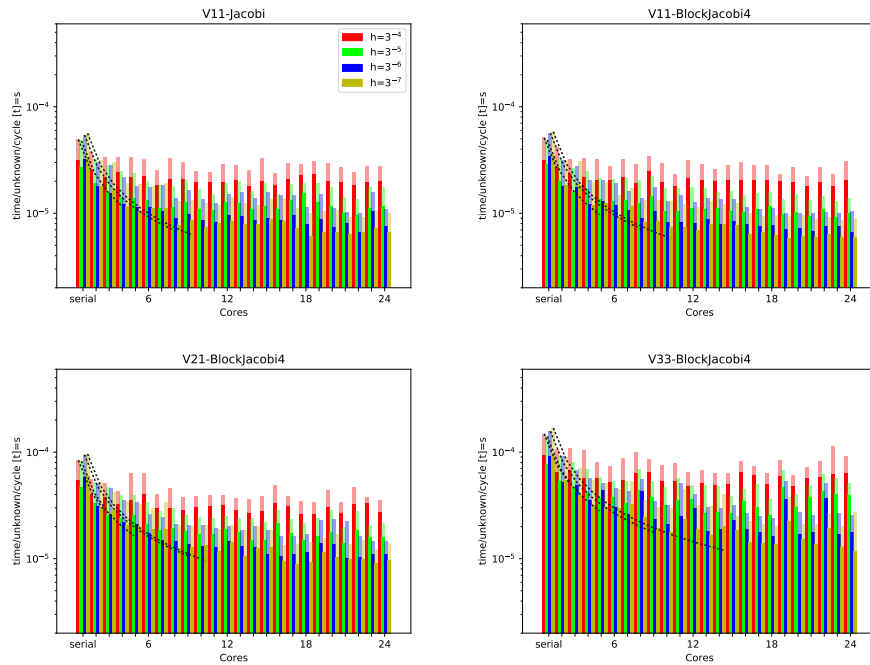


Figure 14: Performance of one cycle of the multiplicative BoxMG solver on the Broadwell for the **sin** benchmark and  $d = 2$ . The dotted line illustrates linear speedup (100% efficiency) truncated by the minimum runtime cost obtained. Each measurement consists of two bars. The bar in the background (lighter, higher runtime) uses  $\epsilon_{mf} = 10^{-8}$ . No compression is used for the measurement in the foreground.

coarse grid problems are introduced. Finally, the runtime penalty of the on-the-fly compression on a single core is pessimistically bounded a factor of two (cmp. Table 13).

Once we use more than one core, the compression yields better speedups than a plain implementation. The arithmetic intensity per grid entity is higher due to the computation of  $\hat{R}$ ,  $\hat{P}$  and  $\hat{A}$  and the pressure on the memory subsystem is lower. Yet, this speedup improvement cannot close the gap between the code with compression and without compression completely. As the theoretical concurrency of the scheme increases with additional grid levels, the speedup increases with an increase of levels. We observe a significant strong scaling behaviour manifested by the fact that bigger problems for large thread counts outperform smaller problems. We further observe that the more smoothing sweeps the better the scalability. Again, this is due to the fine grid which parallelises best. Block smoothers in general have comparably high arithmetic intensity and thus improve the scalability. At the same time, block data accesses and inter-grid transfer operators however reduce the concurrency level.

**Observation 19** *For  $d = 2$ , block smoothers are for free in terms of computational cost. Cost-per-vertex models that are linear in the number of smoothing steps and agnostic of the mesh size are inappropriate here. The cost for data compression has to be evaluated carefully for any application though the technique seems to be promising for manycores. Overall, the scalability is very limited; an effect due to the low order of the discretization inducing a low arithmetic intensity and the rigorous task formalism that introduces a higher administrative overhead than classic for loop-based parallelism.*

Overall, scalability and performance are limited. On all cores, Stream TRIAD [38] yields 3,346.99 MFlops/s with a total used bandwidth of 57,838.15 MBytes/s for the machine. The present V33 simulation however uses only 7,061.49 MBytes/s bandwidth and yields 317.9540 MFlops/s. Its cache miss rate is 0.73%. Switching on the compression increases the compute load to 650.60 MFlops/s but reduces the bandwidth demands to less than 6,000 MBytes/s. However, the cache miss rate increases to around 30%.

All characteristic data highlight the feasibility character of the study—and thus put the comparisons to PETSc into perspective—where no performance engineering is done, everything is modelled with (tiny) tasks, memory access to the individual stencils held in unoptimised hash maps are scattered, and where we study low order discretisations tackled by multiplicative multigrid cycles coarsening up to the trivial level.

We continue with  $d = 3$  experiments (Fig. 15) and observe some changes in the characteristics: The finer the grid the smaller the cost per degree of freedom. Administrative cost now does amortize while the reduction of vertices per coarsening by a factor of 27 is so significant that the coarse grids’ runtime behaviour has no major impact on the efficiency. The qualitative scalability does not change dramatically, and we continue to see strong scaling stagnation already for reasonably small core counts. Stagnation in the plots however is reached sooner as the maximal grid depths we are able to resolve on a single node are shallower than in the two-dimensional counterpart.

**Observation 20** *For  $d = 3$ , the compression cost is not dominant anymore.*

We finally rerun our experiments on the manycore architecture (Fig. 15). All of our statements qualitatively remain valid. They however change quantitatively. The relative compression cost on the manycore is lower and the code scales to slightly higher core counts. KNL’s SNC-4 mode apparently is a well-suited hardware configuration here which implies that we have to use at least

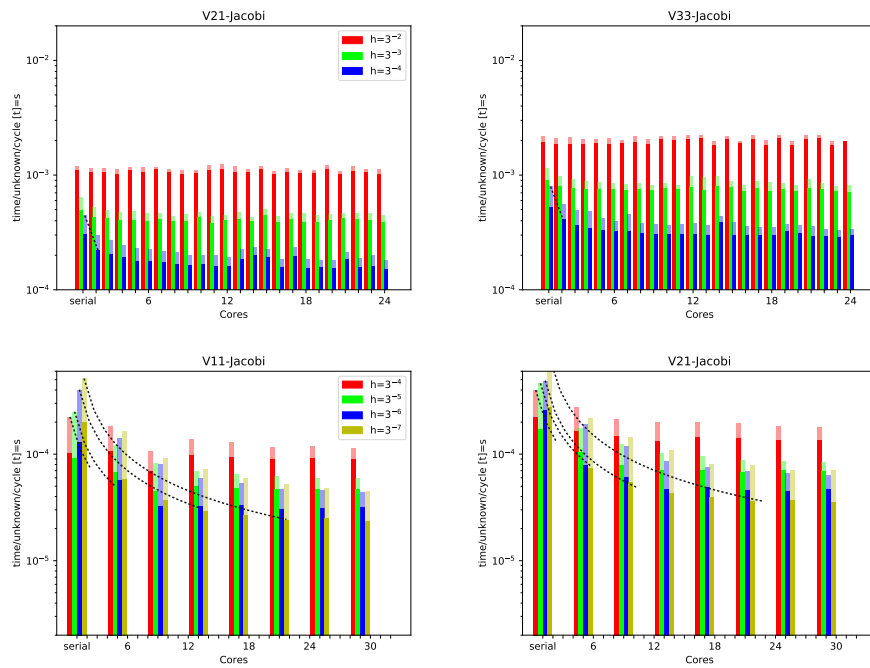


Figure 15: BoxMG on Broadwell for  $d = 3$  (top) and for the KNL for  $d = 2$  (bottom).

Table 14:  $d = 2$  MPI experiments for various node counts (four MPI ranks per node, 24 cores per node) and minimal mesh sizes for V(1,1)-cycles (left) and V(2,1)-cycles (right). All speedups refer to the geometric multigrid variant running on one node with four ranks. Relative to the geometric multigrid baseline, we give the relative cost to compute and maintain the discretisation stencils of BoxMG and, on top of this, do the compression.

#dofs	nodes	$S_{geom}$	stencil cost	comp. cost	$S_{geom}$	stencil cost	comp. cost
$5.91 \cdot 10^4$	1	1.00	1.06	1.53	1.00	1.37	1.44
$5.31 \cdot 10^5$	1	1.14	1.14	1.57	1.13	1.14	1.58
	8	7.74	2.59	1.16	7.74	2.66	1.13
	16	9.41	2.81	1.18	9.41	2.84	1.16
	64	31.29	5.18	1.08	33.35	5.22	1.09
$4.78 \cdot 10^6$	1	1.23	1.01	1.72	1.22	1.00	1.68
	8	9.20	1.43	1.44	9.06	1.43	1.42
	16	11.40	1.55	1.44	11.31	1.60	1.40
	64	61.33	3.19	1.21	59.74	3.15	1.20
$4.31 \cdot 10^7$	8	9.78	1.06	1.78	9.69	1.07	1.74
	16	12.11	1.25	1.76	11.84	1.28	1.47
	64	54.91	1.38	1.65	52.39	1.26	1.45
$3.87 \cdot 10^8$	16	12.92	1.18	1.89	12.83	1.20	1.83
	64	59.30	1.00	2.21	62.22	1.27	1.53

four MPI ranks per node. We summarize that the architecture seems to be even more sensitive to the tasking overhead as the single-core performance difference does not directly relate to the difference in clock speed. Yet, the chip benefits from our data compression more significantly.

For our subsequent MPI experiments, we restrict to  $(\mu_{pre}, \mu_{post}) = (1, 1)$  and  $(\mu_{pre}, \mu_{post}) = (2, 1)$ . Both are challenging choices in terms of scalability as the arithmetic work is small compared to the inter-grid operator evaluations and grid level changes. For the  $(\mu_{pre}, \mu_{post}) = (2, 1)$ , we explicitly exchange all residuals plus stencil contributions per smoothing step, i.e. we anticipate the data flow from a non-linear problem and ignore the fact that the first smoothing step does not have to exchange partial stencils. For the decomposition, we naively apply graph partitioning on the start grid chosen reasonably fine such that it can accommodate all MPI ranks. Any dynamic load balancing is switched off. We have validated that the partitioner yields perfectly balanced subdomains for regular grids. All cost per degree of freedom and, thus, all speedups are normalized to the run with the smallest problem size. Following our shared memory results, we deploy four MPI ranks per node.

We obtain a reasonable scalability  $S_{geom}$  of the geometric baseline code for both cycles once the problem sizes are sufficiently big (Table 14): When we increase the problem size, all grid administration overhead gets amortized. This effect materializes in classic weak speedup, and it also materializes in speedups for serial runs bigger than the minimum mesh size.

The merger of algebraic multigrid’s stencil storage into the geometric code increases the serial runtime slightly. Holding the stencil within the grid also reduces the scalability for the majority of the setups, i.e. the cost grows if we use multiple nodes. More data has to be piped through the communication network. The bandwidth demands increase. This notably is problematic once we run into a strong scaling regime. For very large problems with higher node counts, the stencil administration and communication penalty is not that significant. Stencil compression increases

the runtime further, but this relative increase decreases, for the majority of the setups, with growing node counts. The scheme releases stress from the communication network.

## 8 Conclusion and outlook

This paper proposes a, to the best of our knowledge, new combination of multigrid techniques and novel implementation concepts for quasi-matrix-free geometric-algebraic multigrid on dynamically adaptive grids. First, we apply the BoxMG principle to additive and BPX-type solvers together with HTMG and, thus, are able to support vertical integration and dynamically adaptive grids without any constraints on the frequency of the grid refinement or transition of refinement regions. Second, we discuss an on-the-fly stencil compression that brings together the robustness of BoxMG with the memory modesty of geometric rediscrretization. There are efficient matrix storage schemes for dynamically adaptive formats [34], but our approach goes beyond that as it analyzes the operators themselves. It also reduces the amount of data exchanged between multiple ranks. Finally, we sketch, as third methodological contribution, the impact of the proposed algorithms on parallel programming. The resulting family of solvers is a hybrid between algebraic and geometric multigrid and a hybrid between matrix-free and stencil-holding techniques. A third flavour of hybrid—purely algebraic solvers on coarse grids or forests supplemented by geometric grid hierarchies on finer levels—would fit to the proposed concepts.

While the realization idioms are elegant and the concept of mirroring the arising BoxMG equation systems to a reference configuration makes the higher dimensional implementation much less tedious compared to setting up the equation systems straightforwardly, our experiments reveal that the convergence speed for convection-dominated problems deserves additional attention. Next steps are deriving well-suited estimators that autonomously identify a good  $\ell_{max}$  more elegantly and implementing more sophisticated Petrov-Galerkin inter-grid transfer operators. The most important multigrid shortcoming of the present work is the restriction to Jacobi and block Jacobi smoothers. This restriction results from a single-touch single-traversal doctrine in combination with the element-wise tree traversal. As such, the present studies have academic character, and it is important in the future to weaken the single-sweep paradigm if it renders it possible to realize stronger smoothers. Candidates for suitable smoothers are 2-sweep Krylov schemes [5] or red-black Gauss-Seidel with pipelining which combines multiple sweeps [26]. While giving up on single touch harms implementational elegance, it might even turn out to be favourable from a parallelization point of view to run over the grid multiple times as long as the rank-local work increases faster than the exchanged data cardinality.

Finally, we emphasize a solver property that deserves particular attention: the studied class of low order discretizations yields compact stencils with relatively low arithmetic intensity. Such stencil codes can, in the context of iterative solvers, significantly benefit from careful tuning such as diamond tiling. However, most tunings require invariant stencils in order to perform [37]. Our work targets problems where stencil entries are not constant. At the same time, it is able to compress data automatically in areas where stencils are known a priori. It therefore seems to be promising to inject state-of-the-art stencil techniques for those regions where the compression pays off and to preserve the present approach’s robustness everywhere else.

With the obtained solver robustness our approach widens the class of (sub)systems that can be solved with a spacetree-based multigrid solver significantly, while it preserves the structuredness and low memory footprint properties of geometric multigrid solvers. The software concept thus can become an enabler to solve challenging PDE problems on the grand scale where structuredness is

important to optimize and parallelize and memory (per core) is a precious resource. To achieve this, state-of-the-art techniques from computer science and numerical linear algebra had to be merged into one realization concept.

## Acknowledgements

This work made use of the facilities of the Hamilton HPC Service of Durham University. Furthermore, we particularly have been benefitting from the support of the RSC Group who granted us early access to their KNL machines. Thanks are due to Hans-Joachim Bungartz for supervising and mentoring the underlying PhD theses. It was Irad Yavneh's suggestion to use the idea of BoxMG in this context, and first steps into this direction were made in [61]. Marion wants to thank him for hosting her research stay at Technion which laid the foundations for the present work. Operator and data compression is a workpackage in the ExaHyPE project and Tobias thus appreciates support received from the European Unions Horizon 2020 research and innovation programme under grant agreement No 671698 (ExaHyPE). All underlying software is open source [57].

## References

- [1] M. F. ADAMS, J. BROWN, M. KNEPLEY, AND R. SAMTANEY, *Segmental refinement: A multigrid technique for data locality*, SIAM Journal on Scientific Computing, (2016).
- [2] ADVANCED SCIENTIFIC COMPUTING ADVISORY COMMITTEE (ASCAC) SUBCOMMITTEE, *The Opportunities and Challenges of Exascale Computing*, 2010.
- [3] A. ALONAZI, G. MARKOMANOLIS, AND D. KEYES, *Asynchronous task-based parallelization of algebraic multigrid*, in Proceedings of the Platform for Advanced Scientific Computing Conference, PASC '17, ACM, 2017, pp. 5:1–5:11.
- [4] M. BADER, *Space-Filling Curves - An Introduction with Applications in Scientific Computing*, vol. 9 of Texts in Computational Science and Engineering, Springer-Verlag, 2013.
- [5] M. BADER, S. SCHRAUFSTETTER, C. A. VIGH, AND J. BEHRENS, *Memory efficient adaptive mesh generation and implementation of multigrid algorithms using sierpinski curves*, International Journal of Computational Science and Engineering, 4 (2008), pp. 12–21.
- [6] A. B. BAKER, R. D. FALGOUT, T. V. KOLEV, AND U. MEIER YANG, *Multigrid Smoothers for Ultraparallel Computing*, SIAM Journal on Scientific Computing, 33 (2011), pp. 2864–2887.
- [7] S. BALAY ET AL., *PETSc Web page*. <http://www.mcs.anl.gov/petsc>, 2016.
- [8] P. BASTIAN, W. HACKBUSCH, AND G. WITTUM, *Additive and multiplicative multi-grid : a comparison*, Computing, 60 (1998), pp. 345–364.
- [9] A. BEHIE AND P. A. FORSYTH, JR., *Multi-grid solution of three-dimensional problems with discontinuous coefficients*, Appl. Math. Comput., 13 (1983), pp. 229–240.
- [10] A. BRANDT, *Multi-level Adaptive Solutions to Boundary-Value Problems*, Mathematics of Computation, 31 (1977), pp. 333–390.

- [11] ———, *Multigrid Techniques: 1984 Guide with Applications to Fluid Dynamics*, 1984.
- [12] H.-J. BUNGARTZ, W. ECKHARDT, T. WEINZIERL, AND C. ZENGER, *A precompiler to reduce the memory footprint of multiscale pde solvers in c++*, *Future Generation Computer Systems*, 26 (2010), pp. 175–182.
- [13] C. BURSTEDDE, L. C. WILCOX, AND O. GHATTAS, *p4est: Scalable algorithms for parallel adaptive mesh refinement on forests of octrees*, *SIAM Journal on Scientific Computing*, 33 (2011), pp. 1103–1133.
- [14] D. CHARRIER AND T. WEINZIERL, *An experience report on (auto-)tuning of mesh-based pde solvers on shared memory systems*, in *Parallel Processing and Applied Mathematics, PPAM 2017*, R. Wyrzykowski, J. Dongarra, K. Karczewski, and J. Wasniewski, eds., 2017. (accepted).
- [15] A. CLEARY ET AL., *Robustness and scalability of algebraic multigrid*, *SIAM J. Scientific Computing*, 21 (2000), pp. 1886–1908.
- [16] J. E. DENDY, *Black Box Multigrid*, *Journal of Computational Physics*, 48 (1982), pp. 366–386.
- [17] ———, *Black Box Multigrid for Nonsymmetric Problems*, *Applied Mathematics and Computation*, 13 (1983), pp. 261–283.
- [18] ———, *Two Multigrid Methods for Three-Dimensional Problems with Discontinuous and Anisotropic Coefficients*, *SIAM Journal on Scientific and Statistical Computing*, 8 (1987), pp. 673–685.
- [19] ———, *Black Box Multigrid for Periodic and Singular Problems*, *Applied Mathematics and Computation*, 25 (1988), pp. 1–10.
- [20] J. E. DENDY AND J. D. MOULTON, *Black Box Multigrid with Coarsening by a Factor of Three*, *Numerical Linear Algebra with Applications*, 17 (2010), pp. 577–598.
- [21] J. DONGARRA ET AL., *A proposed api for batched basic linear algebra subprograms*, Tech. Rep. 2016.25, University of Manchester, 2016.
- [22] J. DONGARRA, J. HITTINGER, ET AL., *Applied Mathematics Research for Exascale Computing*, tech. rep., 2014. DOE ASCR Exascale Mathematics Working Group: <http://www.netlib.org/utk/people/JackDongarra/PAPERS/doe-exascale-math-report.pdf>.
- [23] W. ECKHARDT, R. GLAS, D. KORZH, S. WALLNER, AND T. WEINZIERL, *On-the-fly memory compression for multibody algorithms*, in *Advances in Parallel Computing 27: International Conference on Parallel Computing (ParCo) 2015*, G. Joubert, H. Leather, M. Parsons, F. Peters, and M. Sawyer, eds., vol. 27, IOS Press, 2016, pp. 421–430.
- [24] W. ECKHARDT AND T. WEINZIERL, *A Blocking Strategy on Multicore Architectures for Dynamically Adaptive PDE Solvers*, in *Parallel Processing and Applied Mathematics, PPAM 2009*, R. Wyrzykowski, J. Dongarra, K. Karczewski, and J. Wasniewski, eds., vol. 6068 of LNCS, Springer-Verlag, 2010, pp. 567–575.
- [25] C. FEICHTINGER, S. DONATH, H. KÖSTLER, J. GÖTZ, AND U. RÜDE, *WaLBerla: HPC software design for computational engineering simulations*, *Journal of Computational Science*, 2 (2011), pp. 105–112.

- [26] P. GHYSELS AND W. VANROOSE, *Modeling the performance of geometric multigrid stencils on multicore computer architectures*, SIAM Journal on Scientific Computing, 37 (2015), pp. C194–C216.
- [27] B. GMEINER, H. KÖSTLER, M. STÜRMER, AND U. RÜDE, *Parallel multigrid on hierarchical hybrid grids: a performance study on current high performance computing clusters*, Concurrency and Computation: Practice and Experience, 26 (2014), pp. 217–240.
- [28] B. GMEINER, U. RÜDE, H. STENGEL, C. WALUGA, AND B. WOHLMUTH, *Towards textbook efficiency for parallel multigrid*, Numerical Mathematics: Theory, Methods and Applications, 8 (2015), pp. 22–46.
- [29] M. GRIEBEL, *Zur Lösung von Finite-Differenzen- und Finite-Element-Gleichungen mittels der Hierarchischen-Transformations-Mehrgitter-Methode*, PhD thesis, TU München, 1990.
- [30] ———, *Multilevelmethoden als Iterationsverfahren über Erzeugendensystemen*, habilitation thesis, TU München, 1994.
- [31] M. GRIEBEL AND G. ZUMBUSCH, *Parallel Multigrid in an Adaptive PDE Solver Based on Hashing and Space-filling Curves*, Parallel Computing, 25 (1999), pp. 827–843.
- [32] L. B. HART, S. F. MCCORMICK, A. O’GALLAGHER, AND J. W. THOMAS, *The Fast Adaptive Composite-Grid Method (FAC): Algorithms for Advanced Computers*, Applied Mathematics and Computation, 19 (1986), pp. 103–126.
- [33] T. HUCKLE, *Compact fourier analysis for designing multigrid methods*, SIAM Journal on Scientific Computing, 31 (2008), pp. 644–666.
- [34] J. KING, T. GILRAY, R. M. KIRBY, AND M. MIGHT, *Dynamic sparse-matrix allocation on gpus*, in Proceedings ISC High Performance 2016, 2016, pp. 61–80.
- [35] C. LU, X. JIAO, AND N. M. MISSIRLIS, *A hybrid geometric + algebraic multigrid method with semi-iterative smoothers*, Numerical Linear Algebra with Applications, 21 (2014), pp. 221–238.
- [36] S. P. MACLACHLAN, J. D. MOULTON, AND T. P. CHARTIER, *Robust and Adaptive Multigrid Methods: Comparing Structured and Algebraic Approaches*, Numerical Linear Algebra with Applications, 19 (2012), pp. 389–413.
- [37] T. MALAS, G. HAGER, H. LTAIEF, AND D. KEYES, *Multi-dimensional intra-tile parallelization for memory-starved stencil computations*, arXiv:1510.04995, (2015).
- [38] J. D. MCCALPIN, *Memory bandwidth and machine balance in current high performance computers*, IEEE Computer Society Technical Committee on Computer Architecture (TCCA) Newsletter, (1995), pp. 19–25.
- [39] S. F. MCCORMICK, *Multilevel Adaptive Methods for Partial Differential Equations*, Frontiers in Applied Mathematics, SIAM, 1989.
- [40] M. MEHL, T. WEINZIERL, AND C. ZENGER, *A cache-oblivious self-adaptive full multigrid method*, Numerical Linear Algebra with Applications, 13 (2006), pp. 275–291.

- [41] J. D. MOULTON, J. E. DENDY, AND J. M. HYMAN, *The Black Box Multigrid Numerical Homogenization Algorithm*, Journal of Computational Physics, 142 (1998), pp. 80–108.
- [42] B. REPS AND T. WEINZIERL, *A complex additive geometric multigrid solver for the helmholtz equations on spacetrees*, ACM Transactions on Mathematical Software, (2016). accepted.
- [43] J. RUDI, A. C. I. MALOSSI, T. ISAAC, G. STADLER, M. GURNIS, P. W. J. STAAR, Y. INEICHEN, C. BEKAS, A. CURIONI, AND O. GHATTAS, *An extreme-scale implicit solver for complex pdes: Highly heterogeneous flow in earth’s mantle*, in Proceedings of the International Conference for High Performance Computing, Networking, Storage and Analysis, SC ’15, New York, NY, USA, 2015, ACM, pp. 5:1–5:12.
- [44] R. S. SAMPATH, S. S. ADAVANI, H. SUNDAR, I. LASHUK, AND G. BIROS, *Dendro: Parallel algorithms for multigrid and amr methods on 2:1 balanced octrees*, in Proceedings of the 2008 ACM/IEEE Conference on Supercomputing, SC ’08, Piscataway, NJ, USA, 2008, IEEE Press, pp. 18:1–18:12.
- [45] M. SCHREIBER, T. WEINZIERL, AND H.-J. BUNGARTZ, *Cluster optimization and parallelization of simulations with dynamically adaptive grids*, in Proceedings Euro-Par 2013, F. Wolf, B. Mohr, and D. an Mey, eds., vol. 8097 of Lecture Notes in Computer Science, Berlin Heidelberg, 2013, Springer-Verlag, pp. 484–496. preprint.
- [46] T. SCOTT, *Multi-grid methods for oil reservoir simulation in two and three dimensions*, Journal of Computational Physics, 59 (1985), pp. 290 – 307.
- [47] Y. SHAPIRA, *Matrix-Based Multigrid*, Kluwer, 2003.
- [48] K. STÜBEN, *Appendix a: An Introduction to Algebraic Multigrid*, in Multigrid, U. Trottenberg, C. W. Oosterlee, and A. Schüller, eds., Elsevier Science Inc., 2001.
- [49] H. SUNDAR, G. BIROS, C. BURSTEDDE, J. RUDI, O. GHATTAS, AND G. STADLER, *Parallel geometric-algebraic multigrid on unstructured forests of octrees*, in Proceedings of the International Conference on High Performance Computing, Networking, Storage and Analysis, SC ’12, Los Alamitos, CA, USA, 2012, IEEE Computer Society Press, pp. 43:1–43:11.
- [50] H. SUNDAR, R. S. SAMPATH, AND G. BIROS, *Bottom-up construction and 2:1 balance refinement of linear octrees in parallel*, SIAM Journal on Scientific Computing, 30 (2008), pp. 2675–2708.
- [51] E. TREISTER AND I. YAVNEH, *Square and stretch multigrid for stochastic matrix eigenproblems*, Numerical Lin. Alg. with Applic., 17 (2010), pp. 229–251.
- [52] U. TROTTEBERG, C. W. OOSTERLEE, AND A. SCHÜLLER, *Multigrid*, Academic Press, 2001.
- [53] M. WEINZIERL, *Hybrid Geometric-Algebraic Matrix-Free Multigrid on Spacetrees*, PhD Thesis, TU München, 2013.
- [54] T. WEINZIERL, *A Framework for Parallel PDE Solvers on Multiscale Adaptive Cartesian Grids*, Verlag Dr. Hut, 2009. PhD thesis.
- [55] T. WEINZIERL, *The peano software - parallel, automaton-based, dynamically adaptive grid traversals*, tech. rep., 2017. arXiv:1506.04496.

- [56] T. WEINZIERL, M. BADER, K. UNTERWEGER, AND R. WITTMANN, *Block fusion on dynamically adaptive spacetree grids for shallow water waves*, *Parallel Processing Letters*, 24 (2014), p. 1441006.
- [57] T. WEINZIERL ET AL., *Peano—a Framework for PDE Solvers on Spacetree Grids*, 2012. [www.peano-framework.org](http://www.peano-framework.org).
- [58] T. WEINZIERL AND M. MEHL, *Peano – A Traversal and Storage Scheme for Octree-Like Adaptive Cartesian Multiscale Grids*, *SIAM Journal on Scientific Computing*, 33 (2011), pp. 2732–2760.
- [59] R. WIENANDS AND H. KÖSTLER, *A Practical Framework for the Construction of Prolongation Operators for Multigrid Based on Canonical Basis Functions*, *Computing and Visualization in Science*, 13 (2010), pp. 207–220.
- [60] I. YAVNEH, *Coarse-Grid Correction for Nonelliptic and Singular Perturbation Problems*, *SIAM Journal on Scientific Computing*, 19 (1998), pp. 1682–1699.
- [61] I. YAVNEH AND M. WEINZIERL, *Nonsymmetric Black Box Multigrid with Coarsening by Three*, *Numerical Linear Algebra with Applications*, 19 (2012), pp. 246–262.

## A Spacetree construction, properties and traversal

All cells of a spacetree  $\mathcal{T}$  with level  $\ell$  span a grid  $\Omega_{h,\ell}$ . Such an  $\Omega_{h,\ell}$  can be ragged, but all cells have exactly the same size. The union of all  $\Omega_{h,\ell}$  yields an adaptive Cartesian mesh  $\Omega_h$ . The recursive construction scheme ensures that the grids  $\Omega_{h,0} \subseteq \Omega_{h,1} \subseteq \Omega_{h,2} \subseteq \dots \subseteq \Omega_h$  are embedded into each other. These grids carry our shape function weights, i.e. we solve

$$\begin{aligned}
 A_\ell(u_\ell + e_\ell) &= b_\ell + A_\ell u_\ell = Rr_{\ell+1} + A_\ell I u_{\ell+1} \\
 &= R(b_{\ell+1} - A_{\ell+1} u_{\ell+1}) + R A_{\ell+1} P I u_{\ell+1} = R(b_{\ell+1} - A_{\ell+1}(id - PI)u_{\ell+1}) \\
 &=: R(b_{\ell+1} - A_{\ell+1} \hat{u}_{\ell+1}) =: R \hat{r}_{\ell+1}
 \end{aligned}$$

on them.

Various efficient strategies for storing and handling spacetrees, i.e., traversing and providing adjacency information, are known—notably in combination with SFCs: storage within (hash) maps [31], serialization/linearization of the whole tree [50], which allows us in our code [57] to encode a tree traversal into a push-back automaton holding all adjacency data [58], on-the-fly computation of neighbours via Morton codes [13], and so forth. All enlisted variants do not store adjacency explicitly and thus avoid memory overhead. In the present paper, we do not restrict ourselves to a particular storage scheme but rely on the generic concept of *multiscale element-wise traversals*.

**Observation 21** *The classic depth-first tree traversal yields a multiscale element-wise traversal of the spacetree’s multiscale grid.*

This observation [40, 58] is important as depth-first interweaves the traversal of multiple scales. Furthermore, a cell is “left” if and only if all of its children have been processed. Such a vertical integration [1] ensures high temporal and spatial data access locality: The probability that a vertex

manipulated by one cell is required soon after again by a neighbouring cell is high—an effect amplified by the usage of space-filling curves to order the children of any refined tree node. We obtain excellent cache behaviour [40].

The resulting element-wise traversal facilitates solely point Jacobi smoothers as outlined in Sect. 3.2. Point Jacobi is a poor choice for many non-trivial parameter combinations in (1). To facilitate more powerful smoothers without giving up data locality or single touch is our motivation to generalize the tree traversal by a *descend* event (Figure 16). In a depth-first traversal code, such an operation makes a recursive step down within the tree and loads all children of a node before it continues recursively—a one-level recursion unrolling [24]. Though this technique allows us to realize inter-grid transfer operators, we stick to vertex-wise transfer operator realizations. Yet, we use *descend* to implement block smoothers.

## B Review of additive multigrid realisation ideas

Geometric additive multigrid with rediscrretization and one Jacobi smoothing step per level fits into the multiscale element-wise traversal once we shift the standard multigrid cycle by half a grid traversal (Algorithm 2) and introduce a helper variable  $d$  for the correction terms: we switch from a fine-to-coarse to a coarse-to-fine grid level enumeration plus backtracking of the call stack. All required matvec entries can be determined on-the-fly per cell. This holds for  $diag(A_\ell)$  extracting diagonal elements from  $A_\ell$  too. Let  $\omega$  be a generic smoothing parameter. In the present paper, we either use a constant  $\omega$  or we damp  $\omega$  exponentially, i.e., we use  $\omega$  on the finest level,  $\omega^2$  on the first correction level,  $\omega^3$  on the next level, and so forth. Within the spacetree paradigm, the smoothing factor is decreased with the number of coinciding vertices on finer levels: the coarser the level, the smaller the smoother impact. Such a vertex count can be realized during the bottom-up steps [42].

Algorithm 2 works out-of-the-box for adaptive grids if we make the operator  $R$  affect only refined vertices and set the nodal value  $u$  in any hanging vertex to the  $d$ -linear interpolant from the coarser levels. Any grid region can be refined dynamically. Textbook multigrid requires higher order interpolation for newly added levels/vertices [52]. We obtain reasonable convergence speed if we assign newly created vertices the linear interpolant and then immediately apply one undamped Jacobi step. Removing vertices works without any additional effort. Textbook multigrid typically demands an exact coarse-grid solve on  $\ell_{max}$ . We either skip exact coarse-grid solves—in this case, we run one Jacobi step on the coarsest level and have to study the deterioration of the convergence speed—or we run Jacobi sweeps on the coarsest grid until the residual there underruns  $10^{-12}$ . Better iterative or direct solvers are more reasonable in many cases. See [5] for a (preconditioned) CG that fits to the present matrix-free paradigm.

Lines 2–4 of Algorithm 2 translate directly into activities that we perform whenever a vertex is read for the first time during a grid traversal. The residual accumulations in line 6 are performed as element-wise operations. All remaining updates must be realized when a vertex is touched for the last time during a multiscale grid traversal. The recursion and the cell-wise updates are concurrent. Their evaluation can be permuted. A depth-first spacetree traversal for example intermixes cell operations with vertex updates on finer levels. Coarse-grid residual evaluations then work with inconsistent nodal approximations  $u$ . Since the fine-grid work updates coarse-grid values during the computation (last branch), some coarser operator accumulations rely on outdated unknown values from the previous traversal that are then updated while the residual is computed. This data inconsistency can be eliminated by an additional helper variable [42].

Starting from the additive multigrid, we can write down a BPX variant with a single-touch policy (Algorithm 3) if we introduce an additional helper variable  $i$  carrying an injection of the fine-grid updates from  $c$ -points. A  $c$ -point is a grid point that also exists on the next coarser level. Any refined vertex coincides with at least one  $c$ -point. Different to additive multigrid, BPX automatically keeps all levels consistent, as each unknown always is updated only on the coarsest grid where a vertex exists. Spatially coinciding vertices on finer levels hold copies of coarse grid weights. As a result,  $\omega$  is level-independent. The present realization is introduced in [42]. For both additive multigrid and BPX, the first grid sweep realizes only a Jacobi smoother on the fine grid. From the second traversal on, each grid sweep realizes one multilevel update and anticipates operations from the follow-up iteration.

## C BoxMG realisation as one linear equation system solve

The following section discusses the operator  $P$  construction.  $R$  is constructed accordingly. We may rewrite BoxMG's per patch operations into a matrix depending on a vector  $s \in \mathbb{R}^{4^d \cdot 3^d}$  that is applied to a vector  $p \in \mathbb{R}^{2^d \cdot 3^d}$ . Here,  $s$  is a collection of the stencil entries of all vertices within a  $4^d$  patch. The stencil entries are enumerated lexicographically. The vector  $p$  contains the prolongation operator's stencil entries of the  $2^d$  affected coarse grid vertices of one patch. The stencil collapsing (cmp. Sect. 4.4) ensures that the affected section of the  $P$  vectors has only the cardinality  $2^d \cdot 3^d$ .

$d = 1$  We start to illustrate our notation and implementational techniques at hands of a 1d setup where obviously BoxMG's collapse idea does not kick in. All enumerations start with 0. We study one patch. Within a patch, we first study the impact of the patch on the prolongation stencil of the left coarse grid vertex  $p = [p_0, p_1, p_2, p_3, p_4]$ . BoxMG will determine the entries  $p = [p_2, p_3, p_4]$ , i.e. only a subset of this stencil is of interest. We reiterate that it yields ones in the centre of the  $P$  stencils, i.e.  $p_2 = 1$ , so we could reduce the  $p$  input further. However, we enforce this central value manually and thus stick to three output values.

BoxMG's per-patch method invocation accepts an input vector  $s \in \mathbb{R}^{4 \cdot 3}$  holding all the stencils of the patch's vertices. Different to the original BoxMG paper and the present manuscript's construction of BoxMG step by step, our implementation computes all  $p$  entries from one equation system

$$C(s)p = f, \quad p, f \in \mathbb{R}^{3^d}$$

with a right-hand side

$$f_i = \begin{cases} 1 & \text{for } i = 1 \text{ and} \\ 0 & \text{otherwise} \end{cases}.$$

The artificial entry 1 will ensure  $p_2 = 1$ . In classic multigrid manuscripts, the formula for prolongation entries  $p$  depends on the system matrix  $A$  on the next finer level. For our BoxMG implementation, we use  $C \cdot A$  as operator of such a formula where the entries of the matrix  $A$  are determined by the stencils  $s$ . It is thus convenient to write  $C(s)$  here. We reiterate that  $C$  depends linearly on  $s$  and thus is a tensor of third order. However, we here write down the tensor as 2nd order tensor, i.e. as matrix, where the inner multiplication is explicitly expressed. 1d BoxMG then reads as

$$\underbrace{\begin{pmatrix} 1 & 0 & 0 \\ s_{1,0} & s_{1,1} & s_{1,2} \\ 0 & s_{2,0} & s_{2,1} \end{pmatrix}}_{C(s)} \begin{pmatrix} p_2 \\ p_3 \\ p_4 \end{pmatrix} = \begin{pmatrix} 1 \\ 0 \\ 0 \end{pmatrix}. \quad (5)$$

Within the patch, we have to determine  $P$  entries for the right coarse grid vertex, too. Instead of setting up a separate equation system for the second coarse grid vertex—a process that becomes tedious for higher dimensions—we mirror all coarse grid computation problems to a reference configuration where the coarse grid operator affected is tied to the left coarse grid vertex. Before we trigger the equation system solve, we replace the entries in (5) with  $s_{i,j} \mapsto s_{3-i,2-j}$ ,  $i \in \{0, 1, 2, 3\}$ ,  $j \in \{0, 1, 2\}$ , i.e. we mirror them within the patch along the x-axis. The indices  $i \in \{0, 3\}$  could be omitted here, but we use them below. After the solve of (5), we mirror the resulting  $p$  entries back onto the  $p$  entries of the right coarse grid vertex:  $p_i \mapsto p_{4-i}$ .

For plain BoxMG, stencils in the corners of patches ( $s_{0,x}$  and  $s_{3,x}$ ) do not influence  $P$ . They could be omitted. We however keep them in our code as it allows us to work with a vector of  $4^d$  stencil entries instead of  $4^d - 2^d$  which simplifies the implementation for  $d \geq 2$ .

$d = 2$  For two dimensions, our per-patch notation can be written down as

$$\begin{pmatrix} id & 0 & 0 \\ \tilde{A}_{\gamma c} & \tilde{A}_{\gamma\gamma} & 0 \\ A_{lc} & A_{l\gamma} & A_{lu} \end{pmatrix} \begin{pmatrix} P_c \\ P_\gamma \\ P_l \end{pmatrix} u_{\ell-1} =: C \cdot \begin{pmatrix} A_{cc} & A_{c\gamma} & A_{cl} \\ A_{\gamma c} & A_{\gamma\gamma} & A_{\gamma l} \\ A_{lc} & A_{l\gamma} & A_{lu} \end{pmatrix} \begin{pmatrix} P_c \\ P_\gamma \\ P_l \end{pmatrix} u_{\ell-1} = \begin{pmatrix} 1 \\ 0 \\ 0 \end{pmatrix},$$

where  $C$  is the collapsing operator acting on the PDE discretization  $A$ , and  $id \in \mathbb{R}^{2^d \times 2^d}$  is the identity. We study only the bottom left vertex. Our enumeration is bottom-up, left-to-right for both the vertices and the stencil entries (Fig. 17). So whenever we write  $s_{i,j}$ ,  $i$  is the vertex number and  $j$  is the entry of the vertex's stencil. For the coarse grid vertex, we can only determine the nine entries  $(\underbrace{p_{12}, p_{13}, p_{14}, p_{17}, p_{18}, p_{19}}_{P_c}, \underbrace{p_{22}, p_{23}, p_{24}}_{P_\gamma}, \underbrace{p_{20}, p_{21}, p_{25}, p_{26}}_{P_l})$ .

Since  $C$  collapses all stencils along patch boundaries, BoxMG translates the inter-grid transfer operator computation into a set of small, decoupled linear equation system solves; one solve per patch. These solves decompose further: For each of the  $2^d$  vertices, we have to determine those  $P$  entries that coincide with the patch. These computations are independent of each other.

With a reference configuration at hand, the  $C$  matrix for  $d = 2$  and the reference configuration reads as

$$\begin{pmatrix} 1 & 0 & 0 & 0 & 0 & 0 & 0 & 0 & 0 & 0 \\ s_{1,0} + s_{1,3} + s_{1,6} & s_{1,1} + s_{1,4} + s_{1,7} & s_{1,2} + s_{1,5} + s_{1,8} & 0 & 0 & 0 & 0 & 0 & 0 & 0 \\ 0 & s_{2,0} + s_{2,3} + s_{2,6} & s_{2,1} + s_{2,4} + s_{2,7} & 0 & 0 & 0 & 0 & 0 & 0 & 0 \\ s_{4,0} + s_{4,1} + s_{4,2} & 0 & 0 & s_{4,3} + s_{4,4} + s_{4,5} & 0 & 0 & s_{4,6} + s_{4,7} + s_{4,8} & 0 & 0 & 0 \\ 0 & 0 & 0 & s_{8,0} + s_{8,1} + s_{8,2} & 0 & 0 & s_{8,3} + s_{8,4} + s_{8,5} & 0 & 0 & 0 \\ s_{5,0} & s_{5,1} & s_{5,2} s_{5,3} & s_{5,4} & s_{5,5} & s_{5,6} & s_{5,7} & s_{5,8} & & \\ 0 & s_{6,0} & s_{6,1} & 0 & s_{6,3} & s_{6,4} & 0 & s_{6,6} & s_{6,7} & \\ 0 & 0 & 0 & s_{9,0} & s_{9,1} & s_{9,2} & s_{9,3} & s_{9,4} & s_{9,5} & \\ 0 & 0 & 0 & 0 & s_{10,0} & s_{10,1} & 0 & s_{10,3} & s_{10,4} & \end{pmatrix}$$

$d = 3$  The  $C$  matrix for  $d = 3$  is too big to write it down here. All routines are however contained within one of the toolboxes (function collections) available for the underlying software Peano [57] from the project's repository.

## D Remarks on the shared memory parallelization

Patch-based strategies [25, 26, 56], where patches of regular grids are embedded into cells, have been applied successfully for spacetrees and facilitate loop parallelism. Such approaches even can be generalized in a multiscale way, where whole regions are tessellated by a cascade of regular grids [27, 28]. Alternatively, we may fix the grid, cut the linearized tree into chunks and distribute those among threads [45].

To obtain reasonable peak performance, such optimizations might become necessary. We do not study them here as they impose grid regularity constraints. Instead, we focus on a task-based parallelisation formalism. Combinations of both techniques seem to be promising to obtain high performance in practice. Furthermore, we note that the mapping of multigrid element activities onto tasks yields a high theoretical concurrency but also yields high task management overhead. To reduce this overhead and, hence, to increase the arithmetic intensity, our tasks have to be merged into bigger task assemblies [45, 56]. The exact choice of the size of such mergers is a non-trivial task [14].

## E Remarks on block smoothers

Block Jacobi can not be used in the coarsening step in the multiplicative algorithm variant as we fuse the computation of the correction's right-hand side with a smoothing step on the new coarse grid. This is possible as the right-hand side on the correction grid is not required to evaluate the element-wise operators. However, a block smoother on the new coarse grid would require such information.

This would not hold if we plugged into an *ascend* operation that integrates into the backtracking steps within the spacetree. Only offering *ascend* however would create a twin problem: block smoothing throughout the coarsening would be possible but block smoothing throughout a prolongation step would become impossible. Combinations of *descend* and *ascend* solve the problem but sacrifice algorithmic simplicity.

BoxMG's stencil collapsing seems to be a natural candidate to realize better block smoothers: If we apply collapsing on  $\gamma$ -points, these points can be subject to a Gauß-Seidel smoother along the  $\iota$ -points of a patch. Yet, we were not able to identify any significant convergence speedup in our numerical experiments for such a smoother variant. This might be different for harder problems.

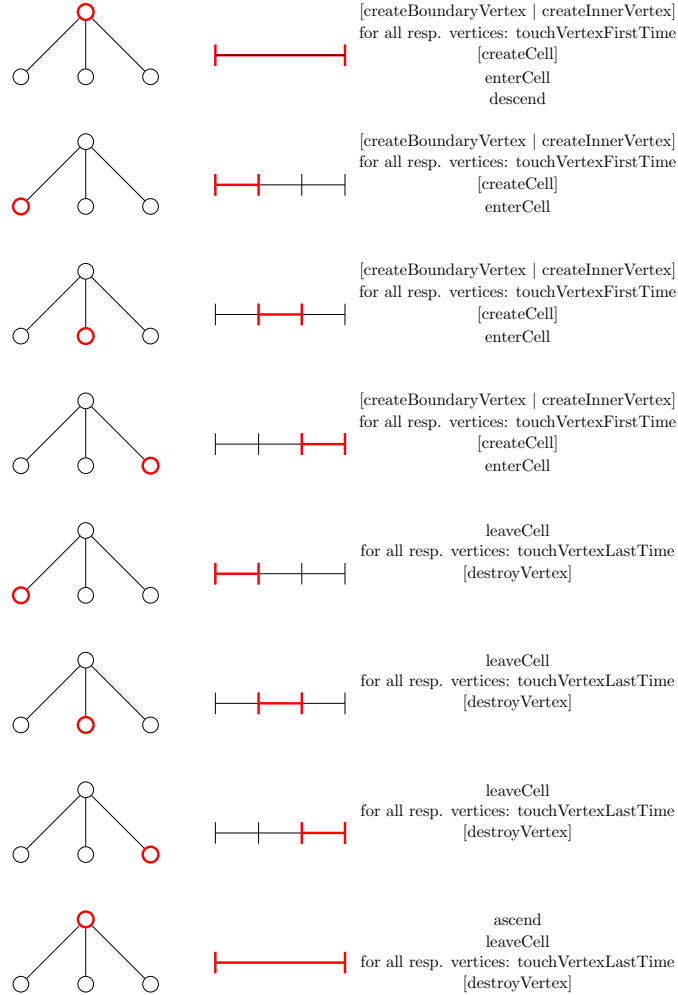


Figure 16: A simple 1D example for the order of (sequential) events during the spacetime traversal (from [53]). The left column shows the tree, the middle column the grid, and the right column the respective events that are called. The current active cell/tree node is highlighted in red. At the beginning of the traversal *beginIteration* and at the end *endIteration* is called. Parallel events and events concerning hanging vertices are omitted. Square brackets stand for events which only occur during the setup/cleanup phase or in an adaptive setting.

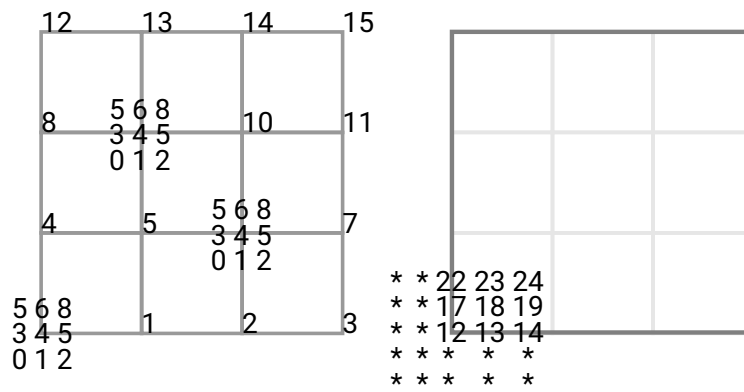


Figure 17: Right: Our BoxMG code computes nine entries of the bottom left vertex for  $d = 2$  within *descend*. Left: All fine grid vertices are enumerated lexicographically starting with 0 at the bottom left (first index subscript). Each vertex carries a  $3^2$  stencil enumerated lexicographically, too.